

LOW MASS PLANETS IN PROTOPLANETARY DISKS WITH NET VERTICAL MAGNETIC FIELDS: THE PLANETARY WAKE AND GAP OPENING

ZHAOHUAN ZHU¹, JAMES M. STONE¹, AND ROMAN R. RAFIKOV¹*Draft version February 15, 2013*

ABSTRACT

We study wakes and gap opening by low mass planets in gaseous protoplanetary disks threaded by net vertical magnetic fields which drive magnetohydrodynamical (MHD) turbulence through the magnetorotational instability (MRI), using three dimensional simulations in the unstratified local shearing box approximation. The wakes, which are excited by the planets, are damped by shocks similar to the wake damping in inviscid hydrodynamic (HD) disks. Angular momentum deposition by shock damping opens gaps in both MHD turbulent disks and inviscid HD disks even for low mass planets, in contradiction to the “thermal criterion” for gap opening. To test the “viscous criterion”, we compared gap properties in MRI-turbulent disks to those in viscous HD disks having the same stress, and found that the same mass planet opens a significantly deeper and wider gap in net vertical flux MHD disks than in viscous HD disks. This difference arises due to the efficient magnetic field transport into the gap region in MRI disks, leading to a larger effective α within the gap. Thus, across the gap, the Maxwell stress profile is smoother than the gap density profile, and a deeper gap is needed for the Maxwell stress gradient to balance the planetary torque density. We also confirmed the large excess torque close to the planet in MHD disks, and found that long-lived density features (termed zonal flows) produced by the MRI can affect planet migration. The comparison with previous results from net toroidal flux/zero flux MHD simulations indicates that the magnetic field geometry plays an important role in the gap opening process. Overall, our results suggest that gaps can be commonly produced by low mass planets in realistic protoplanetary disks, and caution the use of a constant α -viscosity to model gaps in protoplanetary disks.

Subject headings: accretion disks, stars: formation, stars: pre-main sequence

1. INTRODUCTION

During the past decade, exoplanet surveys (e.g. *Kepler*) have greatly advanced our knowledge of the demographics of exoplanets (Howard et al. 2012, Dong & Zhu 2013), which in turn sheds light on planet formation. In the near future, ALMA will directly probe young planets still embedded in gaseous protoplanetary disks. Interpreting such observations will require a better understanding of how planets interact with gaseous disks. In particular, it is well known that planets can excite density waves in disks, which can lead to angular momentum exchange between planets and disks and cause planets to migrate (Goldreich & Tremaine 1979, Ward 1986, Tanaka et al. 2002, Kley & Nelson 2012, and references therein). When these excited waves deposit angular momentum back to the disk, gaps will be opened by planets in disks (Lin & Papaloizou 1979, 1993, Artymowicz & Lubow 1994, Takeuchi et al. 1996, Bryden et al. 1999, Kley 1999). Gap opening is important for understanding both planet migration and growth. After a gap is opened, planet migration slows to the disk viscous timescale (Lin & Papaloizou 1986, Nelson et al. 2000), which is normally referred to as Type II migration. Slowing down of migration is important for the survival of planets on the 10^6 yrs disk life time. Moreover, after a gap opens accretion onto the planet is limited to flow from the circumplan-

etary disk (Lubow et al. 1999 and Lubow & D’Angelo 2006). The circumplanetary disk controls both the final mass of the planet and the formation of planetary satellites (Ward & Canup 2010). A better understanding of each of these topics motivates the study of gap opening in more realistic models of protoplanetary disks.

Conventionally, it is thought that two conditions must be fulfilled simultaneously for a planet to open a gap (Lin & Papaloizou 1993, Bryden et al. 1999). The first is the “thermal criterion”, which states that the planet’s Hill radius needs to be larger than the disk scale height so that the density wave shocks just as it is excited. In other words, the planet mass needs to be higher than the so called - local disk thermal mass

$$M_{th} = \frac{c_s^3}{G\Omega_p} \approx 0.089 M_J \left(\frac{c_s}{0.6 \text{ km s}^{-1}} \right)^3 \left(\frac{M_\odot}{M_*} \right)^{1/2} \left(\frac{R_p}{5 \text{ AU}} \right)^{3/2}, \quad (1)$$

where M_J is the mass of Jupiter, c_s is the disk local sound speed, and R_p and Ω_p are the planet’s semi-major axis and orbital frequency. Recently, this “thermal criterion” for gap opening has been questioned, since even small amplitude waves can still steepen and shock in disks after traveling some distance (Goodman & Rafikov 2001, Rafikov 2002a, Muto et al. 2010, Dong et al. 2011b). This makes possible gap opening by planets with masses significantly lower than the thermal mass M_{th} , see Rafikov (2002b), Li et al. (2009), Duffell & MacFadyen (2012).

The second condition is the “viscous criterion”, which states that the disk viscosity must be low enough for the torque from the planet to overcome the viscous torque.

zhzhu@astro.princeton.edu

¹ Department of Astrophysical Sciences, Princeton University, Princeton, NJ, 08544The movies can be downloaded at <http://www.astro.princeton.edu/~zhzhu/Site/Movies5.html>

Combined with the “thermal criterion”, this requires (Lin & Papaloizou 1993)

$$\frac{M_p}{M_*} \gtrsim \frac{40\nu}{R_p^2 \Omega_p} \quad (2)$$

where ν is the kinematic viscosity of the viscous HD disks. This “viscous criterion” has been analyzed in detail by Crida et al. (2006) through studying the stream lines and a refined formulae was suggested.

An obvious difficulty with the “viscous criterion” is that protoplanetary disks are in fact inviscid; angular momentum transport and accretion are thought to be associated with MHD turbulence driven by the magnetorotational instability (MRI, Balbus & Hawley 1991, 1998 for a review). In ideal MHD the MRI has been extensively studied using both local (Hawley et al. 1995, Stone et al. 1996, Miller & Stone 2000, Davis et al. 2010, Guan & Gammie 2011) and global numerical simulations (Armitage 1998, Hawley 2000, 2001, Fromang & Nelson 2006, Flock et al. 2011, Beckwith et al. 2011). Some aspects of MRI-driven turbulence can be represented by an “ α ” disk model (Shakura & Sunyaev 1973) in a statistical sense (Balbus & Hawley 1991, 1998, Balbus & Papaloizou 1999):

$$\alpha = \frac{T_{MRI}}{\rho_0 c_s^2} = \alpha_{Re} + \alpha_{Max} = \frac{\langle \langle \rho v_x v'_y \rangle \rangle}{\rho_0 c_s^2} - \frac{\langle \langle B_x B_y \rangle \rangle}{4\pi \rho_0 c_s^2} \quad (3)$$

where T_{MRI} is the averaged xy component of the total stress tensor, α_{Re} is the normalized Reynolds stress, α_{Max} is the normalized Maxwell stress, and the double angle brackets $\langle \langle \rangle \rangle$ denotes both time and space averages. However, there is no guarantee that α is a constant in disks with large scale density structures (e.g. gaps). Normally, global simulations (Sorathia et al. 2012) find large α fluctuations at different parts of the disk.

Gap opening by massive planets (much larger than a thermal mass) in MRI-turbulent disks has been studied by several authors using net toroidal flux or zero flux MHD simulations (Winters et al. 2003, Nelson & Papaloizou 2003, Papaloizou et al. 2004, Uribe et al. 2011). Global simulations by Nelson & Papaloizou (2003) suggest the gaps in MRI disks are slightly deeper and wider compared with those in viscous disks, while Winters et al. (2003) found that gaps are slightly shallower in MRI disks. Overall, they found that the shapes of gaps opened by high mass planets are not very different between MRI and viscous disks.

Papaloizou et al. (2004) found that both local shearing box MHD simulations and global MHD simulations show good agreement on the properties of gaps. The local approximation enables high resolution simulations to be carried out. Furthermore, local shearing box simulations can maintain a steady state, which is crucial to study planetary wake and gap properties since some features can only be identified by averaging over hundreds of orbits. Although local simulations lack curvature terms which prohibit studying the differential torque which controls planet migration, it is still possible to study the one-sided Lindblad torque and the gap opening process in the local shearing box approximation as long as the gap structure is sharper than the disk radius R so that the curvature terms are not important.

The tidal torque felt by the planet can be affected by the presence of magnetic fields in disks, which has been studied by linear calculations (Terquem 2003) and numerical simulations (Fromang et al. 2005, Muto et al. 2008). However, these calculations assume strong magnetic fields and non-turbulent disks. It is unclear how MRI turbulence will affect the tidal torque. Recent global MHD simulations have shown some additional torque close to the planet (Uribe et al. 2011; Baruteau et al. 2011). Local shearing box limit is a good way to test if this additional torque is associated with disk global curvatures.

Most previous work on gap opening in MHD disks assumed zero net magnetic flux in simulations. In this paper, we focus on MHD disks with a small net vertical magnetic field. The reason for choosing a small net field is three-fold. First, recent unstratified simulations have shown that the turbulent properties depend on both the numerical resolution and box size with zero net field (Fromang & Papaloizou 2007). Second, simulations with net magnetic flux are more realistic. We expect that small local patches of the disk will be threaded by net vertical fields from molecular clouds, or by toroidal fields generated by the large scale disk dynamo, or even both (Sorathia et al. 2010). Third, by varying the net field strength, we can control the strength of the MRI turbulence, which allows us to systematically study gap opening in disks with various turbulence stresses.

Furthermore, previous work which study gap opening focused on deep gaps induced by massive planets (“Jupiter” mass range). Here we are interested in cases where gaps just start to open in order to test the “thermal” and “viscous criterion”. This motivates us to focus on gap opening by low mass planets (“earth” mass range).

This paper is organized as follows. In §2, we introduce our methods. To provide a benchmark for comparison, we first study gap opening in inviscid hydrodynamic (HD) disks in §3, while planetary wake properties and gap opening in MRI-driven turbulent disks is presented in §4. Gap opening criteria are discussed in §5. After discussions in §6, we conclude the paper in §7.

2. METHOD

2.1. Basic Equations

This study uses Athena (Stone et al. 2008), a higher-order Godunov scheme for MHD with piecewise parabolic method (PPM) for spatial reconstruction, the corner transport upwind (CTU) method for multidimensional integration, and the constrained transport (CT) to conserve the divergence-free property for magnetic fields (Gardiner & Stone 2005, 2008). The simulations are set up as isothermal unstratified disks in the local shearing box approximation (Hawley et al. 1995, Stone & Gardiner 2010), in which the MHD equations are solved in a reference frame centered at radius R_0 corotating with the disk at orbital frequency $\Omega_0 = \Omega(R_0)$. Ignoring curvature terms, the isothermal MHD equations are

$$\frac{\partial \rho}{\partial t} + \nabla \cdot (\rho \mathbf{v}) = 0, \quad (4)$$

$$\frac{\partial \rho \mathbf{v}}{\partial t} + \nabla \cdot (\rho \mathbf{v} \mathbf{v} + \mathbf{T}_B + \mathbf{T}_v) + \nabla p = 2q\mathbf{x}\rho\Omega_0^2\hat{\mathbf{i}} - 2\Omega_0\hat{\mathbf{k}} \times \rho \mathbf{v}, \quad (5)$$

$$\frac{\partial \mathbf{B}}{\partial t} - \nabla \times (\mathbf{v} \times \mathbf{B}) = 0 \quad (6)$$

where p is the gas pressure, the magnetic stress tensor \mathbf{T}_B is

$$\mathbf{T}_B = (B^2/2)\mathbf{I} - \mathbf{B}\mathbf{B}, \quad (7)$$

and the shear parameter q is

$$q = -\frac{1}{2} \frac{d \ln \Omega^2}{d \ln r}, \quad (8)$$

so that for Keplerian flow $q=3/2$. Note that these equations are written in units which assume the magnetic permeability $\mu=1$. An equation of state for an isothermal gas $p = c_s^2 \rho$ is used.

Note that, for HD disks, we have included explicit viscosity in the momentum equation, through the viscous stress tensor \mathbf{T}_v

$$\mathbf{T}_{v;ij} = \nu \rho \left(\partial_i v_j + \partial_j v_i - \frac{2}{3} \partial_k v_k \delta_{ij} \right). \quad (9)$$

where ν is the kinematic viscosity. This allows us to study HD models with viscosity, and compare these to the MHD models which are always inviscid.

An orbital advection scheme (Masset 2000) has been implemented in Athena (Stone & Gardiner 2010). The y -direction momentum equation is split into a linear operator for advection with the background flow velocity, as well as the MHD equations for the velocity fluctuations. The orbital advection scheme significantly accelerates the simulation since the maximum allowed time step is limited by the magnitude of the velocity fluctuations instead of the orbital velocity. It also reduces the inhomogeneous truncation error produced by differential rotation (Johnson et al. 2008).

Gressel & Ziegler (2007) have pointed out that the shearing box boundary conditions can destroy conservation, since the integral of the fluxes over the two radial faces are not identical to machine precision. However, in order to model the density structure (gap formation) in the disk, it is important that the total mass is conserved to round-off error. Thus, we have used the remap scheme similar to Stone & Gardiner (2010) for the density fluxes. First, we remap the radial component of the mass flux at each radial face. Then, we use the arithmetic average of the radial mass flux computed for each grid cell at each radial face, and the remapped value of the radial mass flux from the corresponding grid cell on the opposite face, to update the density in the cells next to the boundary. This scheme guarantees the integral of the mass flux is identical at two boundaries in the x -direction.

To simulate the effect of a planet in 3D unstratified shearing box simulations, a line mass (symmetric in the z -direction) is placed at the center of the box. This geometry is identical to the symmetry of 2D HD simulations, but allows MHD turbulence to be modeled in full 3D. For comparison to 2D simulations we average quantities in the z -direction.

The planet potential is smoothed over several grid cells to avoid small time steps associated with the divergence

of a point source. Following Dong et al. 2011a, we use fourth order smoothing

$$\Phi_p(d) = -GM_p \frac{d^2 + 3R_s^2/2}{(d^2 + R_s^2)^{3/2}}, \quad (10)$$

where d is the distance to the z -axis ($d = \sqrt{x^2 + y^2}$) and R_s is the smoothing length. This potential converges to that of a point mass as $(R_s/d)^4$ for $d \gg R_s$ and deviates from the point mass potential by only 1% at $2.3 R_s$.

Due to the periodic boundary condition, the gradient of the potential has a discontinuity at the boundary. Thus we smooth the potential as

$$\Phi_{s,p}(d) = \Phi_p(d_f) - \sqrt{(\Phi_p(d_f) - \Phi_p(d))^2 + G^2 M_p^2 / R_{so}^2} \quad \text{if } d < d_f \quad (11)$$

and

$$\Phi_{s,p}(d) = \Phi_p(d_f) - GM_p/R_{so} \quad \text{if } d > d_f \quad (12)$$

where d_f is the cut-off radius, beyond which the potential is flat, and R_{so} is a smoothing length at the cut-off radius. For large R_{so} , eq. (11) reduces to (10). With a finite R_{so} the potential becomes flat smoothly (the gradient is a continuous function) at $d = R_{so}$. In all our simulations $d_f = 7.5 H$ and $R_{so} = 50 H$, where H is the disk scale height. With this set-up this potential differs from a point mass potential only by 3.5% at $d_f = 6 H$.

Introduction of the planet potential can disturb the background flow in the disk significantly, and with periodic boundary conditions this initial disturbance can affect later disk evolution. Thus, in HD simulations, we linearly ramp up the amplitude of the planet potential from 0 to 5 orbits, while in MHD simulations, we linearly ramp up the potential from 5 to 10 orbits after the MHD turbulence is established at 5 orbits.

The smoothing length in eq. (10) for simulations with a 0.1, 0.3, and $1 M_t$ planet is chosen as 0.125, 0.18, and 0.269 H respectively, so that the free-fall timescale onto the planet (defined as Eq. 29 of Dong et al. 2011a) is 0.125 in our code units. The numerical time step is fixed at 2×10^{-3} (~ 60 times smaller than the free fall timescale) even though the orbital advection scheme allows for a much longer time step. This small time step allows us to trace the fluid motion around the planet accurately enough to avoid unsteady fluid motion (Dong et al. 2011a). With Athena, Dong et al. (2011a) found, for the case they studied (with resolution 64 grid points per scale height), that the numerical time step needs to be at least 140 times smaller than the free fall timescale onto the planet. While it is clear from physical grounds the time step must be smaller than the free fall time near the planet to properly resolve orbital motion of gas near the planet, the exact ratio between the time step and the free fall time can vary between different codes (Kley et al. 2012). By exploring a larger parameter space, we have also found that the critical time step is roughly proportional to the grid size, as one might expect from the CFL condition. Thus, with a factor of 2 lower resolution in our simulations (32 grid points per scale height as discussed below), the critical time step can be 70 times smaller than the free fall timescale. We have run HD simulations with our choice of parameters and confirmed

that all the runs are stable for 400 orbits with the same boundary set-up in Dong et al. (2011a).

2.2. Model Set-up

We have carried out both 2-D HD (inviscid and viscous) and 3-D MHD simulations with a 0.1, 0.3, and 1 thermal mass (M_{th}) planet at the box center. The code units are chosen as $c_s = 1$, $\Omega = 1$, and $\rho_0 = 1$, so that the disk scale height (H) and the thermal mass (M_{th}) are both 1. The numerical resolution is 32 grid points per H , and the box size is $16 H \times 16 H \times 1 H$ in most simulations. The parameters of the simulations are summarized in Tables 1 and 2. We divide the simulations into one of the three categories.

1) Inviscid 2-D HD simulations with various box sizes and a 0.1 M_{th} planet in the disk. This set of simulations is designed to test whether linear waves launched by the planet will steepen into shocks within the simulation domain, and whether shocks entering from the radially periodic boundary conditions significantly affect the gap region. We use these simulations to determine the ideal box size for further study.

2) 3-D unstratified ideal MHD simulations with and without planets. Simulations without planets allow us to study density fluctuations and turbulent stress due only to the MRI. These calculations serve as a reference for comparison to simulations with planets in order to distinguish, for example, the density dip due to a gap opened by a planet from that associated with zonal flows due to the turbulence (Johansen et al. 2009, Simon et al. 2012).

MHD simulations with different mass planets (0.1, 0.3 and 1 M_t) have been studied. Two different initial vertical field strengths have been applied with $\beta_0=400$ and 1600 (the ratio between the initial gas pressure and the magnetic pressure), leading to disk MHD turbulence with $\alpha=0.17$ and 0.085. The initial net vertical flux is conserved in these simulations. In ideal MHD, the wavelength for the fastest growing linear MRI mode is $H/\lambda = 0.109\beta_0^{1/2}$ (Hawley et al. 1995). With $\beta_0=400$, and 1600, our vertical box size (H) fits 2 and 4 wavelengths of the fastest growing mode. With 32 grids per H , the most unstable wavelength is resolved by 16 and 8 grid cells respectively. This is sufficient to ensure the properties of the MRI-driven turbulence are numerically converged (Hawley et al. 2011, Simon et al. 2009, Sorathia et al. 2012).

3) 2-D viscous HD simulations with constant kinematic viscosity that have the same $R - \phi$ stresses as those in MHD simulations. The gap structures in these viscous disks are compared with the gaps in the MHD simulations from 2) above. The planet masses are again 0.1, 0.3 and 1 M_{th} . Note that in viscous disks the xy component of the viscous stress tensor $T_v \sim \nu \rho (\partial v_y / \partial x + \partial v_x / \partial y) \sim \nu \rho_0 1.5 \Omega$. Equating T_v with the MRI stress $T_{MRI} \sim \alpha \rho_0 c_s^2$ leads to $\nu = \alpha c_s^2 / 1.5 \Omega$. For an example, in order to compare with the MHD run M10B400 which has $\alpha=0.17$, the viscous run V10 needs to have $\nu=0.17/1.5=0.113$.

2.3. Boundary Conditions

In our simulations, we have chosen the periodic boundary condition in both the x - (radial) and y - (azimuthal)

directions. A periodic boundary condition is natural in the azimuthal direction (y or θ). However, applying it to the radial direction effectively introduces an infinite grid of virtual planets at integer spacings of the radial box size. A more natural radial boundary condition would be outflow, or the wave damping condition used by de Val-Borro et al. (2006). However, to model MHD turbulence in the local shearing box periodic boundary conditions must be used at both x and y directions. Therefore, in order to study the effect of the x -direction periodic boundary condition on our results, and to choose the optimum domain size, we have calculated three inviscid HD disks (runs I1, I2, I3) having different radial extents: $8H \times 16H$, $16H \times 16H$, and $32H \times 16H$ and a 0.1 M_t planet at the center. These simulations will be discussed in detail in §3, and in the following paragraph we focus on the effect of the boundary condition.

Figure 1 shows the disk surface density contours at 400 orbits for all three simulations (runs I1, I2, I3). The effect of the x -direction periodic boundary condition is most apparent in the smallest box ($8 H \times 16 H$). The wakes from nearby “virtual” planets overlap with the gap region in the box. Multiple stripes appear in this box instead of two clean gaps, and the edge of the gap is close to the x -direction boundaries. While, the biggest box ($32 H \times 16 H$) has the cleanest gap, the intermediate-sized domain ($16 H \times 16 H$) resolves the two gap structure well, with the two gaps well within the simulation domain. Furthermore, the wakes from nearby planets are much weaker than the wake from the planet at the center. Thus, as the best compromise between cost and accuracy, we have chosen $16 H \times 16 H$ as our box size for most other simulations. We note that in both viscous and MHD models presented later, the wakes from “virtual” planets are a lot weaker than those in the inviscid HD model presented here since the wakes are quickly damped either by viscous stress or the MRI turbulence (§4). The box size used in this study is therefore even more suitable in these cases.

3. GAP OPENING IN INVISCID HD DISKS

Figure 1 also questions the “thermal criterion” for gap opening in the inviscid fluid limit. Gaps are opened by a planet with mass significantly smaller than the “thermal mass”. The objection to the “thermal criterion” was first suggested by Goodman & Rafikov (2001), stating that linear waves from a low mass planet ($M_p < M_{th}$) steepen to shocks after they propagate for a distance

$$|x_{sh}| \approx 0.93 \left(\frac{\gamma + 1}{12/5} \frac{M_p}{M_{th}} \right)^{-2/5} H. \quad (13)$$

where γ is the adiabatic index. Shocks efficiently transfer the wave angular momentum to the background flow, and two gaps should gradually open at the distance of $|x_{sh}|$ on each side of the planet. Thus the thermal mass M_{th} is not a gap opening threshold in this nonlinear wave propagation theory. For a $M_p = 0.1 M_{th}$ planet in an isothermal disk ($\gamma=1$), the waves shock at the distance $|x_{sh}| \sim 2.5 H$.

In Figure 1, we clearly see gap opening for a 0.1 M_{th} planet in an inviscid HD disk (runs I1, I2, I3). The gaps are indeed deepest at $|x| \sim x_{sh} \sim 2H$. The gaps are more prominent with bigger boxes since they are less affected

by the boundary conditions, as discussed in §2.3.

Figure 2 shows the space time plot for the disk surface density in run I2 (the same simulation as in the middle panel of Figure 1). The x -axis is the time in units of the orbital period after the planet is inserted while the y -axis is the y -direction (azimuthal) averaged disk surface density across the gap. We can see that two gaps are gradually opened starting at $|x| \sim 2H$, getting deeper and wider with time. For a long time (hundreds of orbits) a ribbon of material is maintained between the gaps, in agreement with the predictions of Rafikov (2002b). This structure appears because density waves do not dissipate in the coorbital region in an inviscid case, and thus angular momentum is not transferred to the disk, leaving the fluid between the gaps essentially unperturbed. The symmetry of the two-gaps structure in our simulations is due to the shearing box geometry, and should be broken in global simulations, as well as if planet is migrating through the disk.

No steady state is reached, since in an inviscid HD disk, there is no torque to balance the torque from shock dissipation. We find that gaps continue to widen and deepen until some instability, possibly the Rossby wave instability (Lovelace & Hohlfeld 1978; Lovelace et al. 1999; Li et al. 2000; de Val-Borro 2007; Lin & Papaloizou 2010), or Rayleigh instability sets in and destroys the ribbon of gas coorbital with the planet. This should finally result in a single gap in a disk, but reaching this state can take long time for a low mass planet in an inviscid disk.

The timescale to open a factor of 2 deep gap is ~ 400 orbits in our local simulations. However, to derive a timescale for gap opening in a realistic disk based on our local shearing box simulations, the time in our simulations needs to be multiplied by $2\pi R/16H$, where R is the distance from the central star to the planet and $16H$ is our box size in y -direction. This is simply due to the fact that the angular momentum injected by the planet to remove all the material per unit radial distance is proportional to the box extent in the y -direction (which should be $2\pi R$ instead of $16H$), while the torque excited by the planet and the amount of shock dissipation per unit radial distance are independent on the box sizes³. Thus, for a global disk with $H/R=0.1$, the timescale to open a gap by a $0.1 M_{th}$ planet is estimated to be $400 \times 2\pi R/16H \sim 1,500$ orbits.

4. GAP OPENING IN MRI DISKS WITH NET VERTICAL FLUX

In this section, we will first study the wake properties and wake damping mechanism in MHD turbulent disks using simulations with low mass planets (e.g. M01B400 and M03B400, §4.1). Then we will compare the gap properties between the MHD turbulent disks and the viscous disks using simulations with more massive planets (e.g. M10B400, M10B1600, §4.2).

The disk surface densities from these simulations are shown in Figure 3 for planet masses of $1 M_t$, $0.3 M_t$, and $0.1 M_t$ (from top to bottom). The left column shows a snapshot in the MHD simulations (runs M10B400, M03B400, and M01B400) at 70 orbits. The turbulent nature of the MRI disk can be clearly seen. Density

waves excited by the MRI turbulence (Heinemann & Papaloizou 2009) are present across the whole simulation domain. The standard deviation for density fluctuations relative to the background density due to the MRI turbulence alone is as large as ~ 0.3 . With such large density fluctuations, both the gap structure and planetary wake are hard to discern. In order to extract the gap and planetary wake from MRI turbulence, we have averaged the disk surface density every orbit from 80 orbits until the end of the calculation (shown in Table 2). These averaged surface densities are shown in the middle column of panels, where both the gap structure and planetary wakes are clearly evident. By comparing to gaps in viscous HD disks (runs V10, V03, V01, the right column of panels), it is clear that the gaps in MRI disks are deeper, which will be further explored in §4.2.

It is important to note that MRI-turbulent disks can produce large scale density structures that persist over tens to hundreds of orbits, called zonal flows (Johansen et al. 2009, Simon et al. 2012), even without the presence of a planet. To distinguish the gap opened by the planet from zonal flow, we show the space-time plot for the y -averaged disk surface density for runs M10B400, M03B400, M01B400 and B400 in Figure 4. The magnitude of density fluctuations produced by zonal flow can be seen in the bottom panel for the MRI disk with no planet case (B400). Clearly, the density dip in the $1 M_t$ planet run (M10B400, the top panel) is much larger in magnitude than the zonal flow, and the position of the gap is close to the planet. Thus we can confidently say that it is indeed a gap induced by the planet in the M10B400 case. Before we study the gap opening process in MHD disks (§4.2), we first need to understand how waves deposit angular momentum in MRI turbulent disks (§4.1).

4.1. Wake Properties

4.1.1. Identifying Wakes

The damping mechanism of propagating waves determines how angular momentum is deposited into the disk and furthermore the gap opening process. Various damping mechanisms have been proposed, including viscous damping (Takeuchi et al. 1996) in viscous disks and shock damping (Goodman & Rafikov 2001) in inviscid HD disks. In this work we will investigate the damping mechanism in the high Reynolds number MHD turbulence expected in real protoplanetary disks.

To identify the shock region, in Figure 5 we have plotted the vertical average of the velocity divergence $\eta \equiv (\Delta x/c_s) \nabla \cdot v$ (using the sound speed and grid spacing to normalize the velocity and length scales respectively) for both MRI disk (B400, bottom panels) and MRI+planet disk (M10B400, top panels). In our simulations, we find $\eta < -0.2$ is a good criterion for identifying strong shocks.

The leftmost panels of Figure 5 show the contours of η at 80 orbits. The next column of panels outline the region where $\eta < -0.2$, while the next column after that show these outlines in every snapshots from 80 to 130 orbits using a 5 orbit interval. Even in the case of no planets (B400), as shown in the bottom panels, sharp density features are present in the MRI-driven turbulent disks. These shocks in MRI disks are consistent with

³ The box needs to be larger than $\sim 4H \times 4H$ so that most of the planetary torque has been excited (Goldreich & Tremaine 1979).

structures explored in Heinemann & Papaloizou (2012). However, due to the random nature of the turbulence, these shocks appear uniformly in the disk (the lower right panel). When a $1 M_{th}$ planet is present in the disk (M10B400), as shown in the upper panels of Figure 5, it excites strong shocks around the planet, and η can be as low as -0.7. For comparison, a planet in a 2-D inviscid HD disk (I10inv) also excites a strong shock (as shown in the upper rightmost panel), and the smallest η is also -0.7. On the other hand, in the equivalent viscous disk simulation (V10), η of the wake is only -0.066, one order of magnitude smaller than that in both the MHD and inviscid HD cases. Thus, we conclude that shock damping is the main wake dissipation mechanism in MRI disks, which is significantly different from viscous damping with a kinematic viscosity.

As shown in the upper panels of Figure 5, the wake's shock position in MRI-turbulent disks varies with time due to the disk turbulence (the second to right panel), which is different from the static shock in inviscid HD case (the rightmost panel). The random fluctuations in the shock position appear to spread it out over a finite distance, even though at any instant in time the shock profile is sharp. As we will show below, the time average density profile of the planetary wake is surprisingly similar to the wake in a viscous disk.

4.1.2. Averaged Wake Density Profile

The one-armed planetary wake, which is located at

$$y_t \approx -sgn(x) \frac{3x^2}{4H}, \quad (14)$$

in the local limit (Goodman & Rafikov 2001), is due to the coherent interference (Ogilvie & Lubow 2002) of all the modes excited by the planet (perturbed quantities $\propto exp[i(m\phi - \omega t) + k_R R]$), each satisfying the WKB dispersion relationship without self-gravity

$$m^2[\Omega(R) - \Omega_p]^2 = \kappa^2 + k_R^2 c_s^2, \quad (15)$$

where κ is the epicyclic frequency ($\kappa = \Omega$ for a Keplerian disk), k_R is the radial wavenumber in the WKB limit, and $\Omega_p = \Omega(R_p)$ is the pattern speed ω/m in the inertial frame.

Since this one-armed wake is the “signpost” of planet-disk interaction, it is worth studying its structure in detail. The density profiles across the wake in the inviscid HD disk have been studied by Goodman & Rafikov (2001), Dong et al. (2011a) and Rafikov & Petrovich (2012). In this work, we will examine the density profiles of the wake in MRI-driven turbulent disks. In a single snapshot, the planetary wake is significantly disturbed by MHD turbulence (as shown in §4.1.1 above). Thus we average the disk surface density at every time step over 100 orbits for the planetary wake to stand out.

In order to compare the wake at different x positions in different simulations, we need to apply some scaling procedures as in Goodman & Rafikov (2001). For HD simulations, the wake density profiles are measured along azimuthal cuts through the disk at $x=0.5, 1, 2, 4 H$, and then we shift the derived one dimensional density profiles in y by y_t given in Eq. (14). We then scale the density to a dimensionless quantity as follows (Goodman & Rafikov 2001): first, the mean azimuthal density at x is

subtracted to derive $\delta\Sigma$. Since $\delta\Sigma$ increases with x in the linear regime due to the angular momentum flux conservation, we normalize $\delta\Sigma$ by $x^{1/2}$. Finally we scale $\delta\Sigma$ by $\Sigma(x)(M_p/M_{th})$, where $\Sigma(x)$ is the y -direction averaged surface density along x . In the linear theory, with this scaling, the density profile should be independent of M_p at a fixed separation x , and the magnitude of the wake density profile should remain constant with increasing $|x|$ (until the wake shocks).

For MHD simulations, the above scaling procedure is similar but the scaling speed now is the fast magnetosonic speed $\sqrt{c_s^2 + v_A^2}$, where v_A is the Alfvén speed, instead of the sound speed (c_s) as in HD cases (Terquem 2003). We find that the MRI saturated states in these simulations have $\beta \approx 4$, thus the fast magnetosonic speed is $1.22 c_s$ and the new length scale is $1.22 H$. Therefore we make the density cuts at $x=(\pm)0.61, 1.22, 2.44, 4.88 H$. Then we shift the one dimensional density profile by

$$y_t = -sgn(x) \frac{3x^2}{4H} \frac{\sqrt{c_s^2 + v_A^2}}{c_s}, \quad (16)$$

similar to Papaloizou et al. (2004). Finally we scale $\delta\Sigma$ by $\Sigma_0(M_p/M'_{th})$ where $M'_{th} = (c_s^2 + v_A^2)^{3/2}/(G\Omega)$ is a new thermal mass defined via the fast magnetosonic speed. Since the resulting density profiles have a slight asymmetry due to zonal flow in the disk, we average the density profiles from both the positive and negative x sides of the disk.

The resulting wake density profiles from a $0.3 M_t$ planet in disks are shown in Figure 6. Solid, dotted and dashed curves are from MHD simulations (M03B400), viscous HD (V03), and inviscid HD simulations (I03inv) respectively. Remarkably, with the new scaling Eq. (16), the averaged density profiles from the MHD case are quite similar to the density profiles in the viscous disk with the same stress. The sharp density profiles in the inviscid HD disk (I03inv) indicate the formation of the strong shock, while the smooth profiles in the viscous case (V03) indicate the viscous damping. However, the smooth density profiles in the MHD case suggest that, although the damping mechanism is the shock damping (§4.1), the temporal fluctuation of the shock position in an MRI-turbulent disk spreads the wake and, in a time-averaging point of view, the shocks in turbulence have similar effects as the viscosity on the averaged wake density profiles.

4.1.3. Averaged Torque

Using the time averaged surface densities $\langle\Sigma\rangle$ from MHD simulations, we can calculate the time averaged torque density $\langle dT/dx \rangle$ from the planet by integrating $\langle\Sigma\rangle\partial\phi/\partial y$ over the y -direction

$$\langle \frac{dT}{dx} \rangle = - \int \langle \Sigma \rangle \frac{\partial\phi}{\partial y} dy. \quad (17)$$

where the cylindrical region centered on the planet within the planet's Hill radius is excluded for the torque calculation since this region should be bound to the planet and co-moving with the planet. Note that we can calculate the torque density by only integrating $\langle\Sigma\rangle$ over y direction instead of integrating $\langle\rho\rangle$ over both y and z directions, since the planetary potential is independent of the z -direction in our calculations.

The averaged torque densities for M10B400, M03B400, and M01B400 are shown in Figure 7 as the solid curves. By comparison, the dashed curves are from inviscid HD simulations (I10inv, I03inv, I01inv), while the dotted curves are from viscous HD simulations (V10, V03, V01). As well known, the torque densities for inviscid HD disks (dashed curves) have peaks around 1 H, due to the torque cutoff (Goldreich & Tremaine 1980, Artymowicz 1993, Rafikov & Petrovich 2012). In contrast to both the inviscid and viscous HD cases, the averaged torque densities from MRI disks have larger peak values at smaller $|x|$. More discussions are in §7.1.

4.2. Deeper and Wider Gaps

As shown in Figure 3, the gaps in MHD-turbulent disks with net vertical flux (M10B400) are significantly deeper and wider than the gaps in viscous disks with the same stress (V10). To be more quantitative, we average the disk surface densities from MHD simulations M10B400 & M10B1600 over both time, and the y - and z -directions to derive the surface density profile along x , and compare them with those from viscous simulations V10 & V10sv, as shown in Figure 8. Due to the large mass concentration in the circumplanetary region around the planet, the region within $|y| < H$ is removed for the averaging. The solid curves are for MHD simulations, while the dotted curves are for viscous HD simulations. For run M10B400 (solid black curves), the ratio between the smallest surface density within the gap and the surface density at the box edge is $\sim 50\%$, while this ratio is $\sim 80\%$ for the viscous run V10 (dotted black curves). With smaller stresses, the gaps in M10B1600 (solid grey curves) and V10sv (dotted grey curves) are both deep, but the gap in the MHD case M10B1600 is still significantly deeper and wider than the corresponding viscous case V10sv.

In order to understand why the gaps are significantly deeper and wider in these MHD cases, we note that the steady-state gap shape is determined by the balance between angular momentum deposited into the disk and the stress from MRI turbulence (or viscosity). For viscous HD disks, this balance can be expressed as

$$-\int \rho \frac{\partial \phi}{\partial y} dy dz - \frac{d \int (\rho v_x v_y) dy dz}{dx} = \frac{d \int -\nu \rho (\partial_x v_y + \partial_y v_x) dy dz}{dx} \quad (18)$$

while for MHD disks, it is

$$-\int \rho \frac{\partial \phi}{\partial y} dy dz - \frac{d \int (\rho v_x v_y) dy dz|_{planet}}{dx} = \frac{d \int (\rho v_x v_y|_{MRI} - B_x B_y / 4\pi) dy dz}{dx} \quad (19)$$

Note that we separate the Reynolds stress in Eq. (19) into two parts: the portion excited by the planet and that excited by MRI turbulence.

Next, we integrate the above equations along x starting from the planet position $x=0$, and then perform an ensemble average for both time and the z -direction. For the viscous HD disk this gives

$$-\int \langle \frac{dT}{dx} \rangle dx - \int \langle \langle \rho v_x v_y \rangle \rangle dy \Big|_0^x = -\int \langle \langle \nu \rho (\partial_x v_y + \partial_y v_x) \rangle \rangle dy \Big|_0^x. \quad (20)$$

while for the MHD disk it gives

$$-\int \langle \frac{dT}{dx} \rangle dx - \int \langle \langle \rho v_x v_y \rangle \rangle_{planet} dy \Big|_0^x = \int \langle \langle \rho v_x v_y|_{MRI} - B_x B_y / 4\pi \rangle \rangle dy \Big|_0^x \quad (21)$$

For the disk region from 0 to x , the left-hand sides of Eq. (20) and (21) represent this region's net gain of angular momentum from the waves excited by the planet. They consist of the integrated torque exerted by the planet (the first term), minus the angular momentum flux of the waves leaving this region (the second term). The right-hand sides of Eq. (20) and (21) represent the net flux of angular momentum into this region carried by viscosity, or by MHD stresses. A steady gap shape is achieved when the two sides of each equation balance.

We integrated the torque density from the same mass planet for both MHD and viscous runs (as derived in §4.1.3), and found that the integrated torques (the first terms on the left-hand sides of Eqs. 20 and 21) are close to each other within 20% difference. Considering the torque density normally is much larger than the planet induced Reynolds stress, the left hand sides of Eqs. (20) and (21) are similar. This suggests that the rate of deposition of angular momentum from the planet to the disk is similar in both MHD and viscous HD disk simulations, and therefore the differences in gap depth between these two cases can only be due to the stress gradient along x (the right hand sides of Eqs (20) and (21)) as shown below.

4.2.1. Viscous versus Maxwell stress

The averaged viscous stresses for the viscous disks (V10, V10sv) and the Maxwell stresses for the MHD disks (M10B400, M10B1600) are shown in the upper right panel of Figure 8. Only xy components of the stresses are shown. By comparing with the density profiles in the upper left panel, we see that the viscous stresses are almost proportional to the densities in the viscous disks (dotted curves). This correlation is expected since the shear in the y direction dominates the stress and the stress can be approximated by $1.5\nu\rho\Omega$. ν and Ω are both constant in viscous disks. However, as shown as the solid curves, in MHD disks, the Maxwell stresses across the gaps are significantly smoother than the density changes. Since the gap shape is not determined by the stress itself but by its gradient along x (Eq. 19), this smoother stress with respect to ρ across the gap means that to maintain the same stress gradient to balance the planetary torque the gap needs to be deeper in the MHD case.

Along the x direction, the smoother profiles of the Maxwell stress compared with the density can also be characterized by dividing the stress with density, or equivalently calculating α parameter (Eq. 3). For the viscous cases, α is almost constant across the gap, as shown in the upper right panels of Figure 9, and the time and yz -direction averaged α is shown as the dotted curves in the lower left panel of Figure 8. For MHD disks with gap opening, α_{Max} increases towards the gap region, as shown in the lower right panel of Figure 9 and the averaged α_{Max} is shown as the solid curves in the

lower left panel of Figure 8, again suggesting that the MHD stress is smoother across the gap than the density or viscous stress. The time and yz-direction averaged magnetic field (net B_z) is also stronger within the gap (the lower right panel of Figure 8).

We also explored cases with different planet masses (e.g. $3 M_t$, $0.3 M_t$), and box sizes (e.g. $32 H$ in y direction), as shown in Figure 10. α_{Max} in these cases all show the same trend of increase towards the gap region, and gaps are again deeper and wider in MRI disks than corresponding viscous cases. The density and α structure in the xy plane for our biggest box simulation (M10B1600b) are shown in Figure 11, which nicely illustrate the turbulent nature of the disk and demonstrate the higher α in the gap region.

In order to quantify this weak stress dependence on the density across the gap, We calculate the deviation of the Maxwell stress along x

$$\frac{\Delta\langle\langle B_x B_y \rangle\rangle}{\langle\langle B_x B_y \rangle\rangle_0} \equiv \frac{\langle\langle B_x B_y \rangle\rangle_x - \langle\langle B_x B_y \rangle\rangle_0}{\langle\langle B_x B_y \rangle\rangle_0} \quad (22)$$

with respect to the deviation of the density ($\Delta\langle\langle\rho\rangle\rangle/\langle\langle\rho\rangle\rangle_0$), as shown in the left panel of Figure 12. Both $\langle\langle B_x B_y \rangle\rangle$ and $\langle\langle\rho\rangle\rangle$ are derived from Figure 8 and Figure 10 and $\langle\langle B_x B_y \rangle\rangle_0$ corresponds to $\langle\langle\rho\rangle\rangle_0 = 1$. For the viscous stress ($T_v = 1.5\nu\rho\Omega$), $\Delta T_v/T_v = \Delta\rho/\rho$. However, for all the MHD cases with net vertical magnetic flux, $\Delta\langle\langle B_x B_y \rangle\rangle/\langle\langle B_x B_y \rangle\rangle_0 = C\Delta\langle\langle\rho\rangle\rangle/\langle\langle\rho\rangle\rangle_0$ where $C \sim 0.25 < 1$, suggesting $\langle\langle B_x B_y \rangle\rangle \propto \langle\langle\rho\rangle\rangle^{0.25}$ across the gap, and indicating the weak dependence of the stress on the density across the gap. Thus, it is possible to use this new relationship between stress and density to construct a viscous disk model to simulate the gap as in the MRI cases. However, we caution that this relationship is only approximately true for these limited cases as shown.

Finally, in order to understand why α_{Max} is larger inside the gap, we test if the empirical relationship between the turbulent Maxwell stress α_{Max} and the plasma $\langle\langle\beta\rangle\rangle$ in MRI saturated states ($\alpha_{Max} \sim 1/2\langle\langle\beta\rangle\rangle$) (Hawley et al. 1995) still stands across the gap locally. This is shown in the right panel of Figure 12, where each point represents a y direction averaged α_{Max} with respect to the averaged $\langle\langle\beta\rangle\rangle$ at each radius x . As x marches towards the center of the gap, the α_{Max} value increases and the $\langle\langle\beta\rangle\rangle$ value decreases. And they tightly following the empirical relationship. The decreasing $\langle\langle\beta\rangle\rangle$ towards the gap suggests that the turbulent magnetic fields are more concentrated in the gap region with respect to the density.

Not only the turbulent magnetic fields, but also the net magnetic fields concentrate to the gap region (the lower right panel of Figure 8). These two evidences suggest efficient global transport of magnetic fields to the low density gap region in MHD disks with net vertical fields.

4.3. Persistence of the gap

As discussed in §4.2.1, the effective α is higher in the gap region in net vertical flux MHD disks. Thus, if the gap depth is similar between MHD and viscous disks, the Maxwell stress in net vertical flux MHD disks will have a smaller gradient than the viscous stress in viscous HD disks. Since it is the stress gradient that determines the

global transport of the angular momentum and mass, any pre-existing density features will behave quite differently among MHD disks and viscous HD disks.

To test this hypothesis, we restart runs M10B1600 and V10l at a time of 50 orbits, when gaps formed by the planet are fully developed, but with planetary potential switched off in the subsequent evolution. The space-time plot for the disk surface densities are shown in Figure 13. As clearly shown in the upper panel, the gap feature in M10B1600 even persists for 50 orbits after the planet disappears, while in viscous disks the gap is quickly closed for ~ 10 orbits comparable to the viscous timescale $(2H)^2/\nu \sim 20$ orbits. This confirms that the stress is uniform in net vertical flux MRI disks, leading to the inefficiency in erasing the preexisting density features in the shearing box.

This result has far reaching implications for the measurement of the “viscous” timescale from the diffusion of density features in observed disks. If the disk is threaded by a vertical magnetic field, the disk evolution timescale will be longer than the “viscous” timescale.

5. GAP OPENING CRITERIA

5.1. “Thermal Criterion”

We have demonstrated that in an inviscid HD disk, a planet with a mass 10 times smaller than the thermal mass can open gaps by shock formation. Unlike gap opening by a massive planet ($\geq 1 M_{th}$) where a single gap is opened around the planet, a low mass planet opens two gaps away from the planet at the position where density waves shock (Eq. 13).

Simulations with a $0.3 M_{th}$ planet embedded (M03B400, M03B1600) start to show gap features around the planet (lower panels in Figure 10). Similar to $1 M_{th}$ mass cases, a smaller α_{Max} leads to a deeper gap. We expect a $0.3 M_{th}$ planet can open a clearer gap in a even less turbulent disk. Thus, we do not confirm the suggestion of Papaloizou et al. (2004) that the thermal mass is a threshold for gap opening. Low mass planets can also open gaps as long as the disk stress is low.

On the other hand, the timescale for gap opening is longer for smaller planets, and eventually the feedback due to migration starts playing an important role in the gap opening process (Ward 1997, Rafikov 2002), which requires global simulations (Li et al. 2009).

In a future paper, we will show that there is also clear evidence that the gap structure not only depends on the absolute value of the stress (α) but also on the field geometry.

5.2. “Viscous Criterion”

The derivation of the traditional “viscous criterion” (Eq. 2) assumes the thermal criterion is satisfied so that the disk scale height is replaced by the planet’s Hill radius. If we relax this assumption, and balance the momentum flux excited by the planet (Goldreich & Tremaine 1980)

$$F_H \approx 0.93(GM_p)^2 \frac{\Sigma_0 R_p \Omega_p}{c_s^3} \quad (23)$$

and the momentum flux due to viscosity

$$\dot{H}_\nu = 3\pi\Sigma\nu R_p^2\Omega \quad (24)$$

the viscous criterion becomes

$$\left(\frac{M_p}{M_*}\right)^2 \gtrsim \frac{10\nu H^3}{R_p^5 \Omega} \sim 6\alpha \left(\frac{H}{R_p}\right)^5. \quad (25)$$

where 6 is just an order of magnitude estimate and the detailed value depends on how we define a “gap”. However, this criterion needs to be modified to study gap opening in the shearing box limit, since the momentum flux due to viscosity in the shearing box is

$$\dot{H}_\nu = 1.5\Sigma\nu R_p\Omega H_y \quad (26)$$

where H_y is the box size in y direction. Thus, the viscous criterion in the shearing box is

$$\left(\frac{M_p}{M_*}\right)^2 \geq \frac{1.6\nu H_y H^3}{R_p^6 \Omega} \sim \alpha \left(\frac{H}{R_p}\right)^5 \frac{H_y}{R_p}, \quad (27)$$

or

$$\left(\frac{M_p}{M_{th}}\right)^2 \geq \frac{1.6\nu H_y \Omega^2}{c_s^3} \sim \alpha \frac{H_y}{H} \quad (28)$$

For a disk having $\nu=0.113$, the viscous criterion requires the planet mass larger than $1.7 M_{th}$ with $H_y = 16H$. This explains why a gap cannot be opened in our HD viscous runs (10% dip in V10). However, a 50% deep gap is opened in our MHD run (M10B400) as discussed in §4.2, suggesting that the viscous criterion needs to be modified, at least for net vertical flux simulations.

5.3. The Comparison with Previous results

Our results are different from previous gap opening studies using net toroidal flux or zero flux MHD simulations (Winters et al. 2003, Nelson & Papaloizou 2003, Papaloizou et al. 2004, Uribe et al. 2011) in respect that previous simulations found similar gap depths between MHD cases and viscous cases⁴. Furthermore, our main result that α_{max} is higher in the whole gap region has not been reported before. Papaloizou et al. (2004) reported the increasing α_{max} along the planetary wake in their Figure 19 & 21. But their Fig 21 suggests that α_{max} decreases in the gap region. These differences between our results and previous results may suggest that different magnetic field geometries in the disk affect the gap opening process.

To confirm that the deeper gaps in our simulations are due to the different field geometry we have applied, we have also carried out gap opening simulations with net toroidal magnetic fields. We have indeed observed similar planet-induced gap depths between net toroidal flux MHD cases and viscous cases, which is consistent with previous studies.

More surprisingly, we found that, in net toroidal flux MHD simulations, α_{max} decreases towards the gap region (consistent with Figure 21 in Papaloizou et al. 2004), which is fundamentally different from the increasing α_{max} towards the gap region in net vertical flux MHD simulations. This result will be presented in a later paper.

⁴ There are some subtle differences in these previous studies. Winters et al. (2003) found gaps are slightly shallower in MRI disks compared with viscous cases, while Nelson & Papaloizou (2003) suggest that gaps are deeper and wider in MRI disks.

6. DISCUSSION

6.1. Torque and Migration

Planet migration is an important result of the planet-disk interaction theory (Goldreich & Tremaine 1980, Lin & Papaloizou 1993). As we have discussed in §4.1.3, interaction with a MHD turbulent disk changes the planetary torque density in comparison to HD cases. More importantly, it causes a “random walk” of the planet when fluctuations of the torque associated with turbulence dominates the Lindblad torque (Nelson & Papaloizou 2004, Uribe et al. 2011).

The time evolution of the total torques for runs M01B400, M03B400, and M10B400 are shown in Figure 14. The torques from both sides of the disk and the net torques are shown. The fluctuating torque is more important for less massive planets (e.g. $0.1 M_t$, M01B400) since the torque from the turbulence is proportional to the planet mass while the Lindblad torque is proportional to the square of the planet mass.

For an intermediate mass planet ($0.3 M_t$, M03B400), the long lasting non-uniform background zonal flow (Johansen et al. 2009, Simon et al. 2012) can also significantly change the migration (Yang et al. 2009, 2012). This is shown in the middle panel of Figure 14 where the net torque is always negative due to the zonal flow, even though it should be zero if the background is uniform in the shearing box limit. This net torque is almost 20% of the total one-sided torque. However, caution has to be made by using shearing box simulations to study both stochastic migration and zonal flows (Yang et al. 2009, 2012), and how zonal flow affects planet migration in global disks needs further study.

It is unclear whether, in a very long time scale, the planet’s stochastic motion can still lead to a one direction migration as in a laminar disk. We can indirectly address this question by averaging the one-sided torque over long times and comparing it with the Lindblad torque in HD disks. As shown in Figure 7, the averaged torques in net vertical flux MHD disks do not equal to the torque in HD disks. An excess torque very close to the planet is present around $0.2-0.3 H$. A similar excess torque is found by Baruteau et al. (2011) (Figure 13) in global simulations.

Several mechanisms can potentially explain this excess torque, such as the “magnetic resonance” (Terquem 2003, Fromang et al. 2005) and the horseshoe motion amplified corotation torque (Guilet et al. 2013). Unfortunately, we did not confirm any of these mechanisms, partly due to the complication of MHD turbulence. For the “magnetic resonance”, We do not observe significantly density features associated with this resonance (Fig. 4 in Fromang et al. 2005). For the MHD corotation torque, our shearing box set-up do not exhibit the shift between the planet and the separatrices by design. This shift is global disks introduces the MHD corotation torque (Guilet et al. 2013). Thus, the mechanism behind this excess torque in our simulations is unclear. Examining Fig. 3 in detail, we find that the circumplanetary region in MHD cases is asymmetric which may indicate some modification by the magnetic field to the circumplanetary region.

6.2. Can we use α to study gap opening?

Although viscous disks have been extensively used to study gap opening and even planet accretion, our work suggests that caution has to be exercised when applying viscous models to real protoplanetary disks.

First, α viscosity models MRI turbulence only in a statistical sense (Balbus & Papaloizou 1999). At any given instant in time, quantities such as the wake profile, gap shape, and torque can be very different in inviscid MHD turbulence compared to a viscous HD disk. This implies that if we are able to resolve the spiral structure induced by planets in protoplanetary disk with ALMA, the spiral arm may be distorted and disjointed which is very different from the smooth structure in viscous HD disks (Fig 3).

Second, even though the stress in MRI turbulent disks can be scaled to the disk pressure in a volume averaged sense, we find that since the turbulent stresses are not proportional to density, possibly due to global transport of magnetic fields, the value of the effective α can vary across the gap region. In our net vertical flux MHD simulations, the gap region has a higher α than the rest of the disk. Calculating accurate models in viscous HD requires varying the value of α . An empirical formulae is presented in §4.2.1. Note that this formulae is derived from our simulations with limited net field strength range, planet mass range, and ignoring dissipation. Particularly, the MHD turbulent strength can be affected by the dissipation coefficients (Lesur & Longaretti 2007, Longaretti & Lesur 2010) even in net vertical field simulations. In order to understand the gap structure in the realistic simulation with dissipation, we need to first understand how magnetic fields are transported in such disks with density features. This demands numerical simulations with very high resolution, which is beyond the scope of this paper.

Finally, properties of the circumplanetary region highly depend on the magnetic field geometry and field strength there, which is not isolated from the rest of the magnetic fields in MHD disks. Although the density around the circumplanetary region is very high due to the gravity of the planet, the magnetic fields could be less affected by the presence of the planet due to the efficient global transport of the magnetic fields. If $\alpha \sim 1/2\beta$ still stands there, the equivalent α in the circumplanetary region could be very small. Moreover, the global geometry of the magnetic field in this region means the stress is not completely local, but there are torques due to connections to the outer gap regions. It is unclear how this can be modeled in the local α formulation.

6.3. Gaps in protoplanetary disks and observational Implications

Current observations cannot constrain the structure of protoplanetary disks accurately due to the limited resolution and disk's large optical depth at infrared. Theoretical calculations considering ionization network (e.g. Bai 2011) suggest the existence of the MRI “dead zone” (Gammie 1996). The stress (or α) can be very low in the “dead zone” making it similar to the inviscid HD disk. Based on our inviscid HD simulations, two gaps can be opened in the disk adjacent to a low mass planet. This “two gap” structure might be observable by ALMA in future.

For MRI active regions in disks, the planet-induced gap

structure depends on how the disk is threaded by global magnetic fields. Disks with net vertical fields have drawn greater attention recently since net vertical fields seem to be essential to produce disk winds and jets (Bai&Stone 2012, Fromang et al. 2012, Lesur et al. 2012). If protoplanetary disks are threaded by net vertical fields, gaps can be opened by lower mass planets in contrast to the viscous HD models.

On the other hand, if a gap is observed, “ α models” may not be accurate enough to use the gap structure to determine the planet mass. Stratified MHD simulations with realistic disk ionization structures are needed. Eventually global MHD simulations are needed to derive a realistic gap shape. Some of these issues will be addressed in our next paper.

Furthermore, the spiral arms produced by the planet can be fragmented by MRI turbulence. In a real protoplanetary disk, the spiral arms can be turbulent and dynamical, and different from the static spiral arms produced in viscous “ α models”.

7. CONCLUSION

We have studied the wake and gap opening by a low mass planet with both two dimensional HD and three dimensional MHD simulations in the unstratified local shearing box limit. Similar to the case of inviscid HD, the density wake launched by a planet steepens into a shock in the MRI turbulent disk. Thus shock dissipation dominates wave dissipation in MHD disks. Turbulent fluctuations cause the shock position to vary in time, and when averaged over hundreds of orbits the random wake positions form a smooth density profile which is remarkably similar to that in viscous disks with the same total stress. On the other hand, we find the average torque density excited by the planet to be different from the torque density in HD simulations: it has a peak around $0.2-0.3 H$ away from the planet compared to $\sim 1 H$ in HD simulations. Furthermore, zonal flow makes the background disk not uniform leading to a net torque even in the local shearing box limit.

We have also studied gap opening criteria in both HD disks and MRI-driven MHD turbulent disks. In inviscid HD disks, we find a 0.1 thermal mass planet can open two gaps at the position where the density waves shock, which subsequently deepen and merge into a single gap structure. This is consistent with the expectation from nonlinear semi-analytical calculations by Goodman & Rafikov (2001) and Rafikov (2002b), but contradicts the generally accepted “thermal criterion” for gap opening. For a disk with $H/R=0.1$, the timescale for this gap opening is around 10^3 orbits. In MHD turbulent disks, we find that a $0.3 M_{th}$ planet can open a 20% deep gap in a disk with equivalent $\alpha=0.08$. Overall, both our HD and MHD results show that gaps can be opened by planets significantly below the thermal mass.

By varying the strength of the initial vertical magnetic fields, we have studied the gap structure in MRI disks with different turbulent amplitudes, and compared the results to viscous HD disks with the same stress. The gaps in MRI disks having net vertical fields are deeper and wider in comparison to viscous HD disks. In particular, we find that, with an initial vertical field $\beta_0 = 400$ in disks, the gap formed by a thermal mass planet contains of a density dip of 2, while only a 10% density

TABLE 1
HYDRODYNAMIC MODELS (2D)

Case name	Box size H×H	Planet mass M_t	Run Time $2\pi/\Omega$	Kinematic Viscosity
Inviscid Disks				
I1	8×16	0.1	400	0
I2	16×16	0.1	400	0
I3	32×16	0.1	400	0
I10inv	16×16	1	20	0
I03inv	16×16	0.3	20	0
I01inv	16×16	0.1	20	0
Viscous Disks				
V01	16×16	0.1	100	0.113
V03	16×16	0.3	100	0.113
V10	16×16	1	100	0.113
V10l	16×16	1	100	0.03
V10sv	16×16	1	100	0.056
V10bsv	16×32	1	100	0.056

dip is observed in the viscous HD disk. This difference in gap shape is due to the fact that the MRI stress (T) across the gap depends only weakly on the density ($\Delta T/T = 0.25\Delta\rho/\rho$ in disks with initial vertical magnetic fields) while the viscous stress is proportional to the density.

Looking at this in a different way, the equivalent α parameter of the MHD turbulence is higher within the

planet-induced gap of net vertical flux MHD disks. Remarkably, the correlation between the total stress measured by α and the plasma β ($\sim 1/2\alpha$) found generally in studies of the MRI (Hawley et al. 1995) still holds even inside the gap. Both turbulent magnetic fields and net vertical magnetic fields are more concentrated in the gap region with respect to the density, suggesting an efficient global transport of magnetic fields into the low density gap which leads to α variation across the gap.

The fact that α is not constant within the gap, and that MHD stresses are not proportional to density across the gap (leading to deeper and wider gaps in MHD) calls into question the use of viscous HD simulations to study gap opening in protoplanetary disks. In the future, in order to model the dynamics of protoplanetary disks more accurately, we will study gap opening in stratified and layered MRI-turbulent disks.

This work was supported by NSF grant AST-0908269 and Princeton University. All simulations were carried out using computers supported by the Princeton Institute of Computational Science and Engineering. We thank Steve Lubow and Xuening Bai for helpful discussions.

REFERENCES

Armitage, P. J. 1998, *ApJ*, 501, L189
 Artymowicz, P. 1993, *ApJ*, 419, 155
 Artymowicz, P., & Lubow, S. H. 1994, *ApJ*, 421, 651
 Bai, X.-N. 2011, *ApJ*, 739, 50
 Bai, X.-N., & Stone, J. M. 2012, *arXiv:1210.6661*
 Balbus, S. A., & Hawley, J. F. 1991, *ApJ*, 376, 214
 Balbus, S. A., & Hawley, J. F. 1998, *Reviews of Modern Physics*, 70, 1
 Balbus, S. A., & Papaloizou, J. C. B. 1999, *ApJ*, 521, 650
 Baruteau, C., Fromang, S., Nelson, R. P., & Masset, F. 2011, *A&A*, 533, A84
 Beckwith, K., Armitage, P. J., & Simon, J. B. 2011, *MNRAS*, 416, 361
 Bryden, G., Chen, X., Lin, D. N. C., Nelson, R. P., & Papaloizou, J. C. B. 1999, *ApJ*, 514, 344
 Crida, A., Morbidelli, A., & Masset, F. 2006, *ICARUS*, 181, 587
 Davis, S. W., Stone, J. M., & Pessah, M. E. 2010, *ApJ*, 713, 52
 de Val-Borro, M., Edgar, R. G., Artymowicz, P., et al. 2006, *MNRAS*, 370, 529
 de Val-Borro, M., Artymowicz, P., D’Angelo, G., & Peplinski, A. 2007, *A&A*, 471, 1043
 Dong, R., Rafikov, R. R., & Stone, J. M. 2011, *ApJ*, 741, 57
 Dong, R., Rafikov, R. R., Stone, J. M., & Petrovich, C. 2011, *ApJ*, 741, 56
 Dong, S., & Zhu, Z. 2012, *arXiv:1212.4853*
 Duffell, P. C., & MacFadyen, A. I. 2012, *ApJ*, 755, 7
 Flock, M., Dzyurkevich, N., Klahr, H., Turner, N. J., & Henning, T. 2011, *ApJ*, 735, 122
 Fromang, S., Latter, H. N., Lesur, G., & Ogilvie, G. I. 2012, *arXiv:1210.6664*
 Fromang, S., & Nelson, R. P. 2006, *A&A*, 457, 343
 Fromang, S., & Papaloizou, J. 2007, *A&A*, 476, 1113
 Fromang, S., Terquem, C., & Nelson, R. P. 2005, *MNRAS*, 363, 943
 Gammie, C. F. 1996, *ApJ*, 457, 355
 Gardiner, T. A., & Stone, J. M. 2005, *Journal of Computational Physics*, 205, 509
 Gardiner, T. A., & Stone, J. M. 2008, *Journal of Computational Physics*, 227, 4123
 Goldreich, P., & Tremaine, S. 1979, *ApJ*, 233, 857
 Goldreich, P., & Tremaine, S. 1980, *ApJ*, 241, 425
 Goodman, J., & Rafikov, R. R. 2001, *ApJ*, 552, 793

TABLE 2
MHD MODELS (UNSTRATIFIED 3D (X=16H, Z=1H))

Case name	Planet mass (M_t)	Run Time $2\pi/\Omega$	Net Field Geometry	Initial Field β_0	stress (α)
Y=16H					
B400	0	200	Vertical	400	0.18
M01B400	0.1	400	Vertical	400	0.17
M03B400	0.3	246	Vertical	400	0.17
M03B1600	0.3	264	Vertical	1600	0.085
M10B400	1	258	Vertical	400	0.17
M10B1600	1	225	Vertical	1600	0.081
M30B400	3	258	Vertical	400	0.12
Y=32H					
M10B1600b	1	138	Vertical	1600	0.084

Gressel, O., & Ziegler, U. 2007, *Computer Physics Communications*, 176, 652
 Guan, X., & Gammie, C. F. 2011, *ApJ*, 728, 130
 Guilet, J., Baruteau, C., & Papaloizou, J. C. B. 2013, *arXiv:1301.2337*
 Hawley, J. F., Gammie, C. F., & Balbus, S. A. 1995, *ApJ*, 440, 742
 Hawley, J. F. 2000, *ApJ*, 528, 462
 Hawley, J. F. 2001, *ApJ*, 554, 534
 Hawley, J. F., Guan, X., & Krolik, J. H. 2011, *ApJ*, 738, 84
 Heinemann, T., & Papaloizou, J. C. B. 2009, *MNRAS*, 397, 64
 Heinemann, T., & Papaloizou, J. C. B. 2012, *MNRAS*, 419, 1085
 Howard, A. W., Marcy, G. W., Bryson, S. T., et al. 2012, *ApJS*, 201, 15
 Johansen, A., Youdin, A., & Klahr, H. 2009, *ApJ*, 697, 1269
 Johnson, B. M., Guan, X., & Gammie, C. F. 2008, *ApJS*, 177, 373
 Kley, W. 1999, *MNRAS*, 303, 696
 Kley, W., & Nelson, R. P. 2012, *ARA&A*, 50, 211
 Kley, W., Müller, T. W. A., Kolb, S. M., Benítez-Llambay, P., & Masset, F. 2012, *A&A*, 546, A99
 Lesur, G., & Longaretti, P.-Y. 2007, *MNRAS*, 378, 1471
 Lesur, G., Ferreira, J., & Ogilvie, G. 2012, *arXiv:1210.6660*
 Longaretti, P.-Y., & Lesur, G. 2010, *A&A*, 516, A51
 Li, H., Finn, J. M., Lovelace, R. V. E., & Colgate, S. A. 2000, *ApJ*, 533, 1023
 Li, H., Lubow, S. H., Li, S., & Lin, D. N. C. 2009, *ApJ*, 690, L52

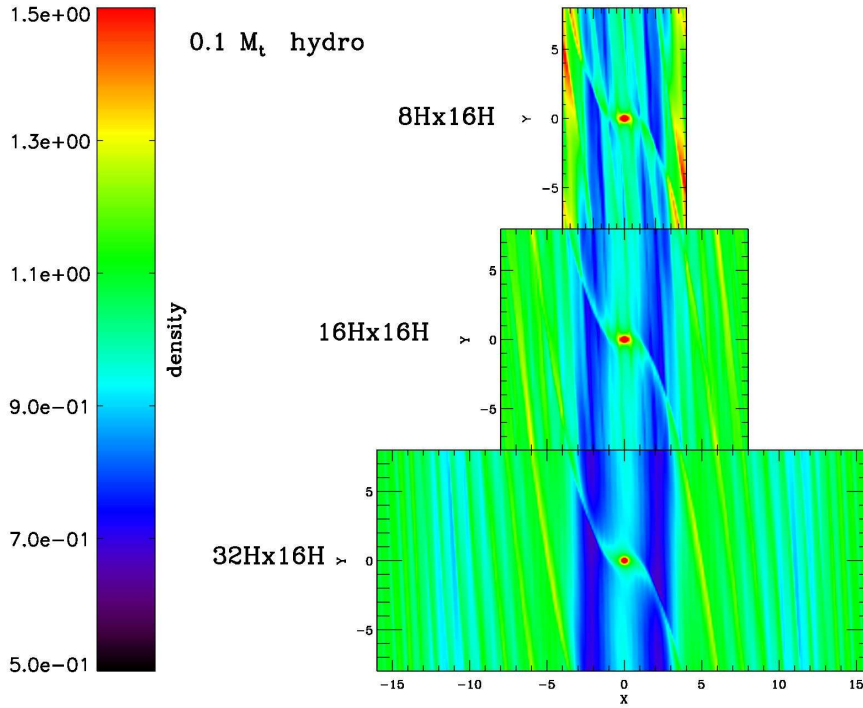


FIG. 1.— The surface density in 2-D inviscid HD disks with a $0.1 M_{\oplus}$ thermal mass planet at the center. Simulations with different box sizes (cases I1, I2, I3) have been shown. The snapshots are taken at 400 orbits. A cleaner gap is seen in a bigger box and the effect of virtual planets from neighbor boxes diminishes. The $16 H \times 16 H$ box shows the gaps clearly and is used for most runs in the paper. The simulations also demonstrate that low mass planets (less than the thermal mass) can open gaps in inviscid HD disks.

- Lin, D. N. C., & Papaloizou, J. 1979, *MNRAS*, 186, 799
 Lin, D. N. C., & Papaloizou, J. 1986, *ApJ*, 309, 846
 Lin, D. N. C., & Papaloizou, J. C. B. 1993, *Protostars and Planets III*, 749
 Lin, M.-K., & Papaloizou, J. C. B. 2010, *MNRAS*, 405, 1473
 Lovelace, R. V. E., Li, H., Colgate, S. A., & Nelson, A. F. 1999, *ApJ*, 513, 805
 Lovelace, R. V. E., & Hohlfield, R. G. 1978, *ApJ*, 221, 51
 Lubow, S. H., Seibert, M., & Artymowicz, P. 1999, *ApJ*, 526, 1001
 Lubow, S. H., & D'Angelo, G. 2006, *ApJ*, 641, 526
 Masset, F. 2000, *A&AS*, 141, 165
 Miller, K. A., & Stone, J. M. 2000, *ApJ*, 534, 398
 Muto, T., Machida, M. N., & Inutsuka, S.-i. 2008, *ApJ*, 679, 813
 Muto, T., Suzuki, T. K., & Inutsuka, S.-i. 2010, *ApJ*, 724, 448
 Nelson, R. P., Papaloizou, J. C. B., Masset, F., & Kley, W. 2000, *MNRAS*, 318, 18
 Nelson, R. P., & Papaloizou, J. C. B. 2003, *MNRAS*, 339, 993
 Nelson, R. P., & Papaloizou, J. C. B. 2004, *MNRAS*, 350, 849
 Ogilvie, G. I., & Lubow, S. H. 2002, *MNRAS*, 330, 950
 Papaloizou, J. C. B., Nelson, R. P., & Snellgrove, M. D. 2004, *MNRAS*, 350, 829
 Rafikov, R. R. 2002, *ApJ*, 569, 997
 Rafikov, R. R. 2002, *ApJ*, 572, 566
 Rafikov, R. R., & Petrovich, C. 2012, *ApJ*, 747, 24
 Shakura, N. I., & Sunyaev, R. A. 1973, *A&A*, 24, 337
 Simon, J. B., Beckwith, K., & Armitage, P. J. 2012, *arXiv:1203.0314*
 Simon, J. B., Hawley, J. F., & Beckwith, K. 2009, *ApJ*, 690, 974
 Sorathia, K. A., Reynolds, C. S., & Armitage, P. J. 2010, *ApJ*, 712, 1241
 Sorathia, K. A., Reynolds, C. S., Stone, J. M., & Beckwith, K. 2012, *ApJ*, 749, 189
 Stone, J. M., Hawley, J. F., Gammie, C. F., & Balbus, S. A. 1996, *ApJ*, 463, 656
 Stone, J. M., Gardiner, T. A., Teuben, P., Hawley, J. F., & Simon, J. B. 2008, *ApJS*, 178, 137
 Stone, J. M., & Gardiner, T. A. 2010, *ApJS*, 189, 142
 Takeuchi, T., Miyama, S. M., & Lin, D. N. C. 1996, *ApJ*, 460, 832
 Tanaka, H., Takeuchi, T., & Ward, W. R. 2002, *ApJ*, 565, 1257
 Terquem, C. E. J. M. L. J. 2003, *MNRAS*, 341, 1157
 Uribe, A. L., Klahr, H., Flock, M., & Henning, T. 2011, *ApJ*, 736, 85
 Ward, W. R. 1986, *ICARUS*, 67, 164
 Ward, W. R. 1997, *ICARUS*, 126, 261
 Ward, W. R., & Canup, R. M. 2010, *AJ*, 140, 1168
 Winters, W. F., Balbus, S. A., & Hawley, J. F. 2003, *ApJ*, 589, 543
 Yang, C.-C., Mac Low, M.-M., & Menou, K. 2009, *ApJ*, 707, 1233
 Yang, C.-C., Mac Low, M.-M., & Menou, K. 2012, *ApJ*, 748, 79

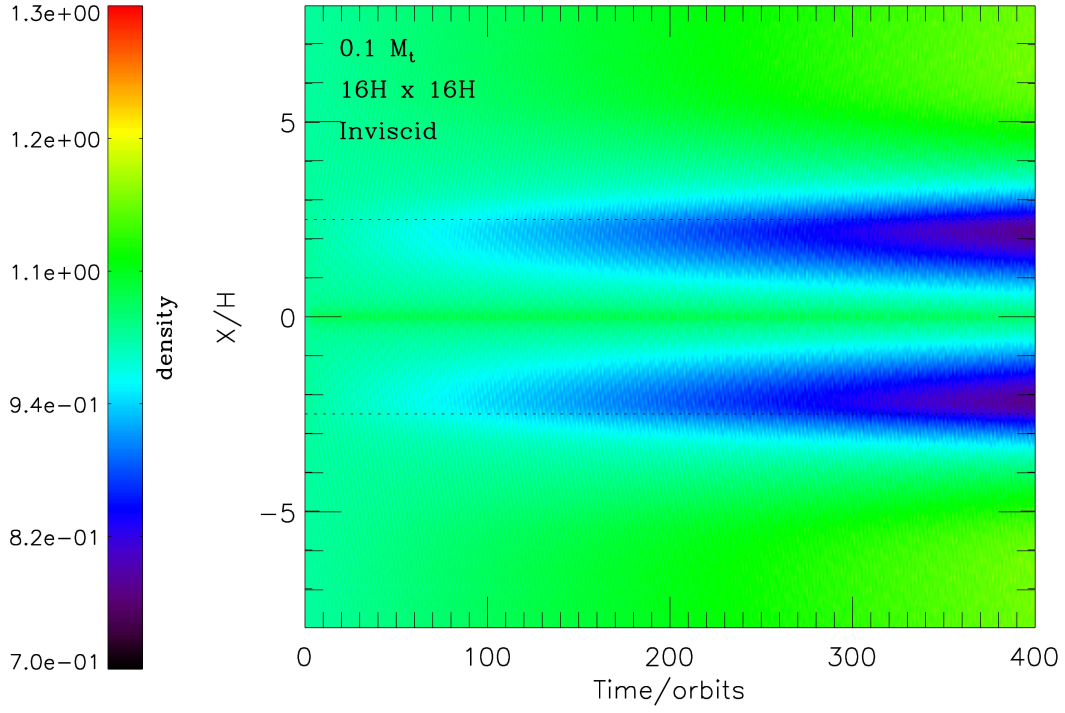


FIG. 2.— The space-time plot for the disk surface density (y -direction averaged) with respect to x in the inviscid HD disk (case I2) having a 0.1 thermal mass planet at the center. X axis is in unit of orbits. Two gaps are gradually opened adjacent to the planet and they get deeper with time. The two dotted lines are where density waves excited by a 0.1 thermal mass planet become shocks.

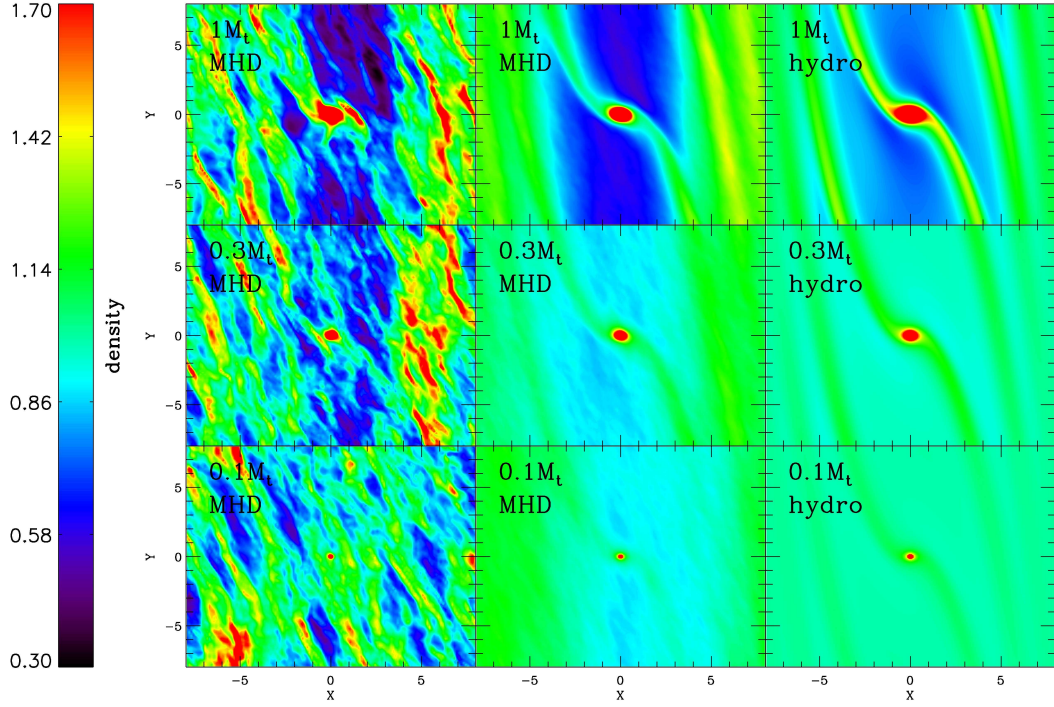


FIG. 3.— The z -direction averaged disk surface densities for MRI turbulent disks (left and middle panels, M10B400, M03B400, M01B400 from top to bottom) and viscous disks (2D) having the same equivalent stress $\alpha=0.17$ as the MRI disks (right panels, V10, V03, V01 from top to bottom). The planets at the box center have different masses: 1 thermal mass in the upper panels, 0.3 thermal mass in the middle panels and 0.1 thermal mass in the lower panels. The left panels are the snapshots of the MHD simulations at a given time while the middle panels are from the same simulations but averaged over hundreds of orbits. Comparing the upper middle and right panels, we can see the gap is deeper in the MHD case.

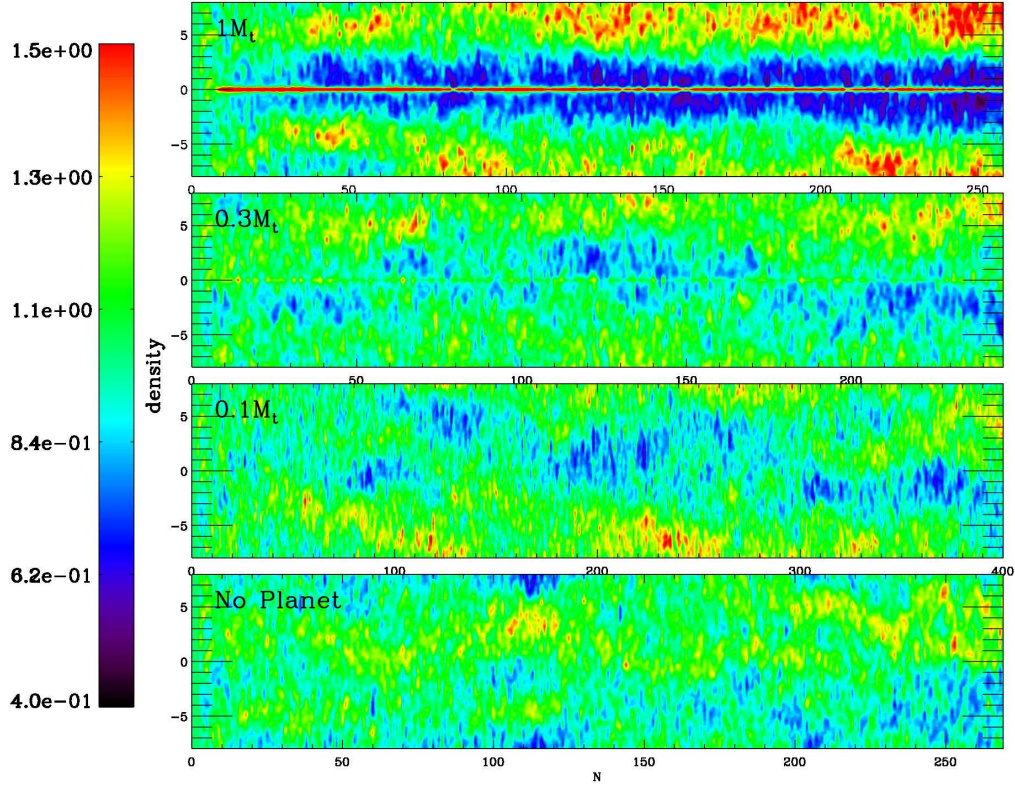


FIG. 4.— The space-time plots of the yz -direction averaged disk surface densities for M10B400, M03B400, M01B400, and B400 (top to bottom panels). A clear gap is opened in the M10B400, while density structures in lower mass cases (asymmetric with respect to $x = 0$) resemble zonal flow from B400 (the bottom panel).

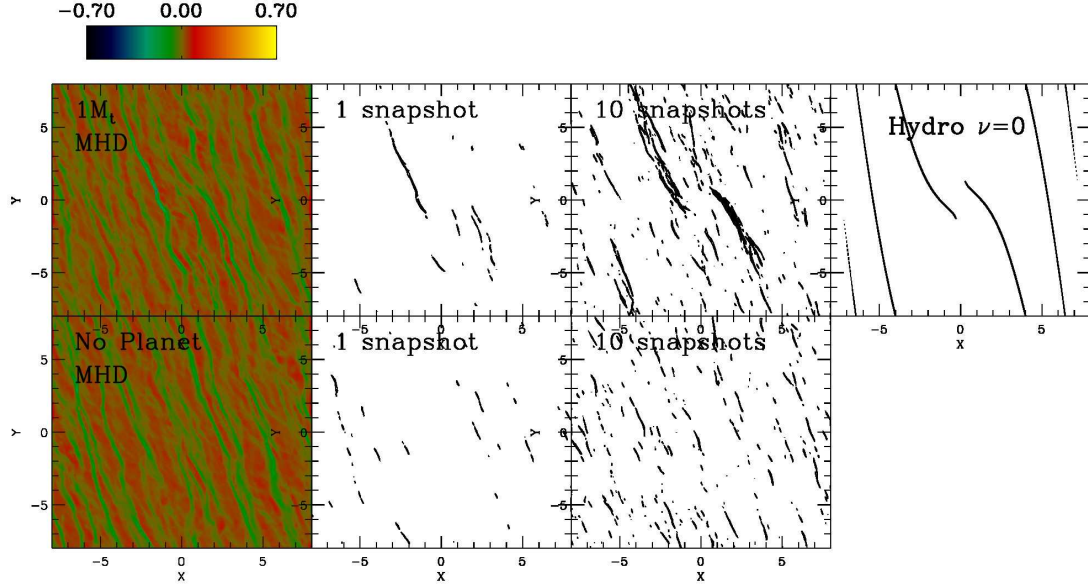


FIG. 5.— The z -direction averaged $(\Delta x/c_s)\nabla \cdot v$ of MRI disks with a 1 thermal mass planet at the center (upper left three panels, M10B400) and the MRI disk without planets (lower panels, B400). The leftmost panels show the color contours of $(\Delta x/c_s)\nabla \cdot v$ at a given time. The second to left panels outline the contours with values smaller than -0.2, which identify the shock regions in disks. The second to right panels overlap these outlines in snapshots from 80 to 130 orbits with 5 orbits interval. The upper right panel shows the same outline for an inviscid HD disk (I10inv). The planetary wake in the MHD case has similar shock strength as the wake in the inviscid HD case, thus in MRI disks the waves are dissipated by shocks. However, since the shock position varies with time, the averaged wake density profiles over hundreds of orbits are a lot smoother as shown in Figure 6.

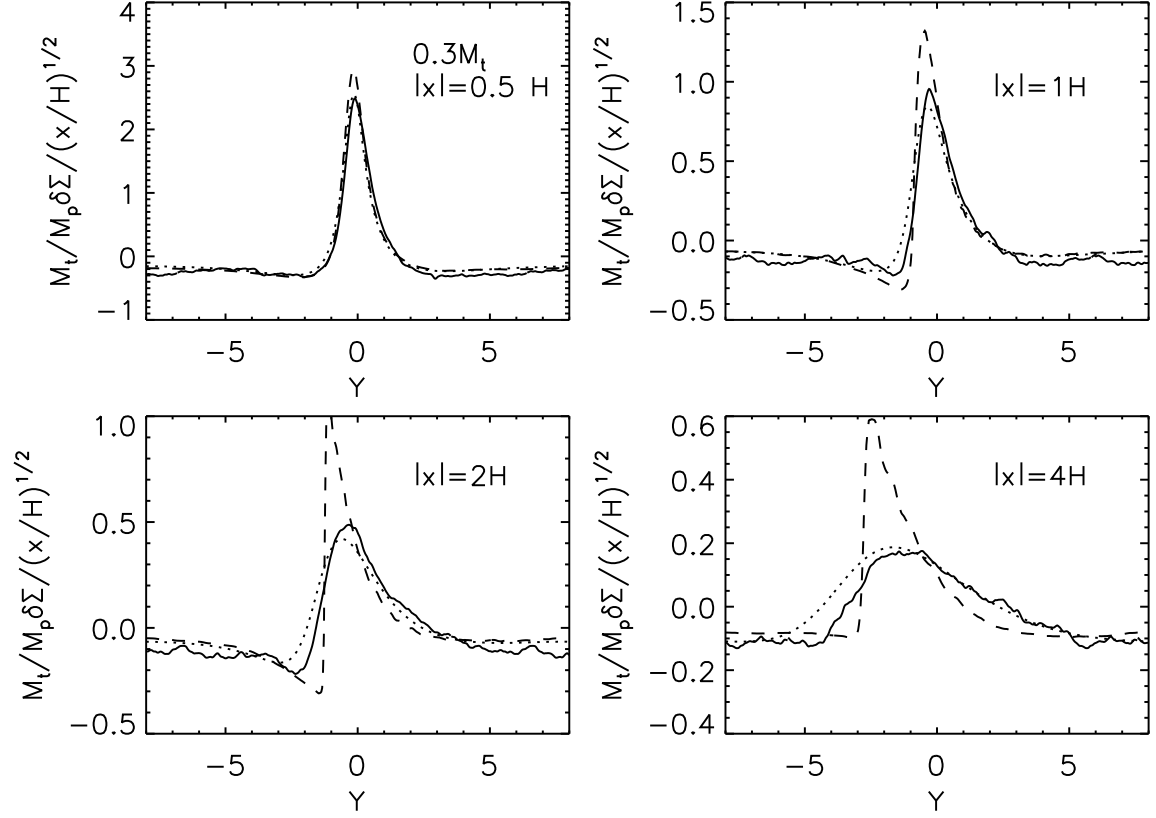


FIG. 6.— The (time and z -direction averaged) surface density profiles along y -direction at $x=0.5, 1, 2, 4$ scale heights away from the planet in inviscid HD (I03inv, dashed curves), viscous (V03, dotted curves) and MHD simulations (M03B400, solid curves). The solid curves are scaled with the fast magnetosonic speed ($\sqrt{c_s^2 + v_A^2}$, detailed in §4.1.2). A remarkably good agreement is found between the averaged density profiles of MHD cases and those of viscous HD cases, even though the wave is dissipated by shocks in MHD cases (Fig. 5).

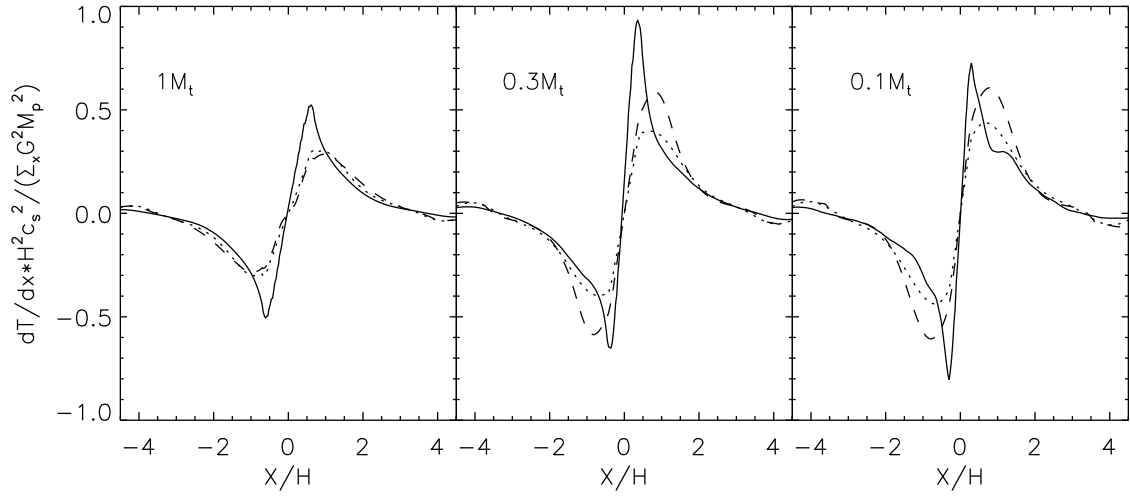


FIG. 7.— The time averaged torque densities excited by a $1 M_t$, $0.3 M_t$, $0.1 M_t$ planet in the disk (from left to right). The solid curves are from MHD simulations (M10B400, M03B400, M01B400). The dotted curves are from viscous HD runs (V10, V03, V01) while the dashed curves are from inviscid HD runs (I10inv, I03inv, I01inv). Torque densities in MRI disks have peaks closer to the planet.

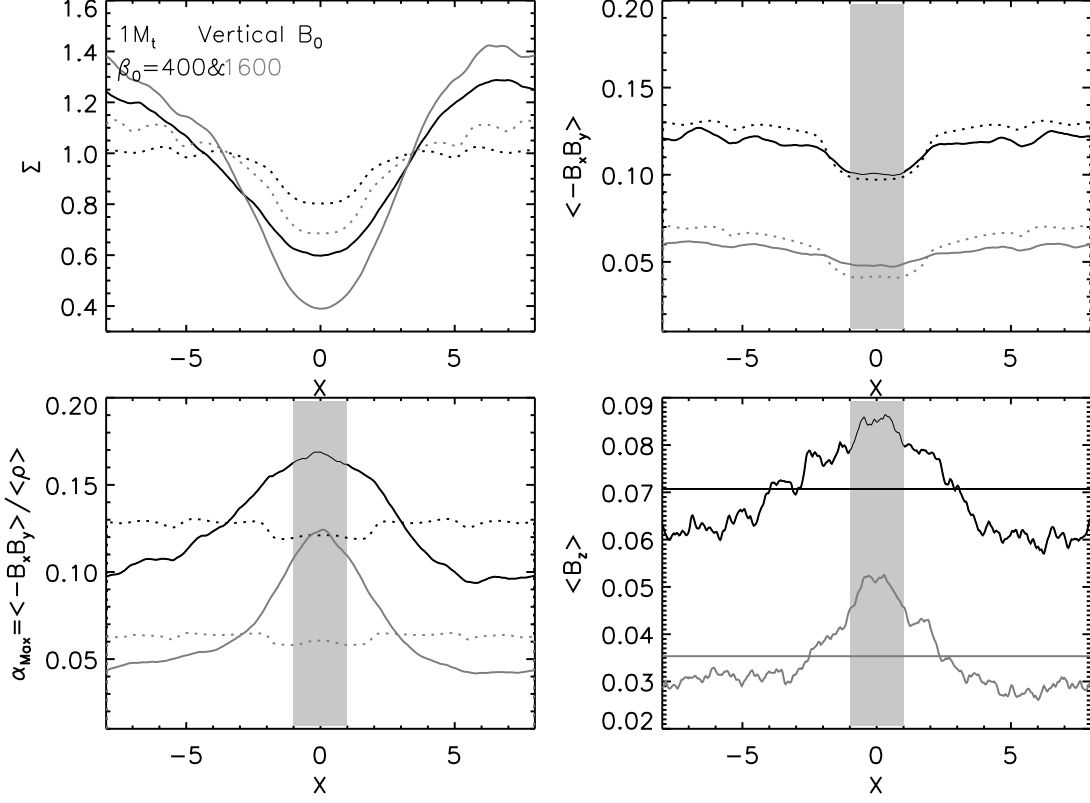


FIG. 8.— The yz -direction and time averaged disk surface densities (upper left panel), Maxwell Stress (upper right panel), equivalent α_{Max} (lower left panel), and net vertical flux (lower right panel) for vertical net flux MHD simulations with a 1 thermal mass planet at the box center. Regions closing to the planet ($|y| < H$) are masked out for the averaging. $|x| < H$ is shown in the upper right and lower panels as the shaded region. Two different initial field strengths have been applied (M10B400(dark curves) and M10B1600 (light curves)). The equivalent viscous cases(V10sv, V10st) are over-plotted as the dotted curves. In order to be compared with the Maxwell stress and α_{Max} , the viscous stress (T_{xy}) and α are multiplied by 3/4 in these plots. Clearly, the gaps are significantly deeper in MHD cases than the viscous cases since in MHD cases the stress is flat compared to the density, or, in other words, α increases towards the gap region. In the lower right panel, the initial vertical field strengths are plotted as the flat solid lines. Net magnetic fields are concentrated in the gap region.

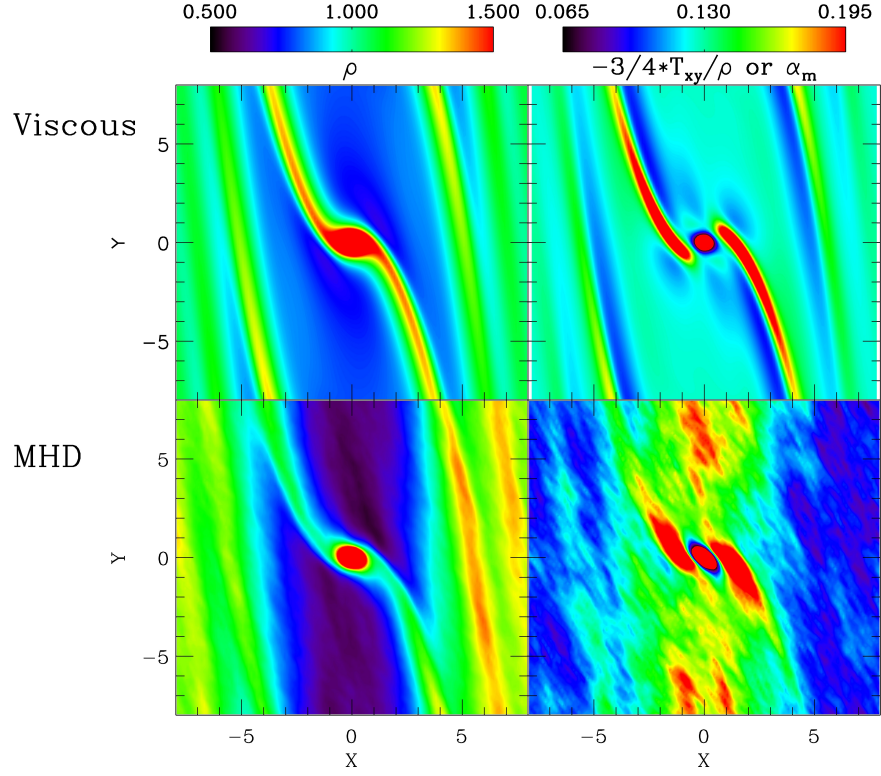


FIG. 9.— The disk surface density (left panels), and the ratio between the stress and density (α , right panels) for viscous (V10, upper panels) and MHD (M10B400, lower panels) cases. For the MHD case, xy component of the stress is the Maxwell stress. For the viscous case, the viscous stress (T_{xy}) is multiplied by 3/4 to be compared with the Maxwell stress. Compared with the viscous case, the stress-density ratio (α) in the MHD case is higher in the gap.

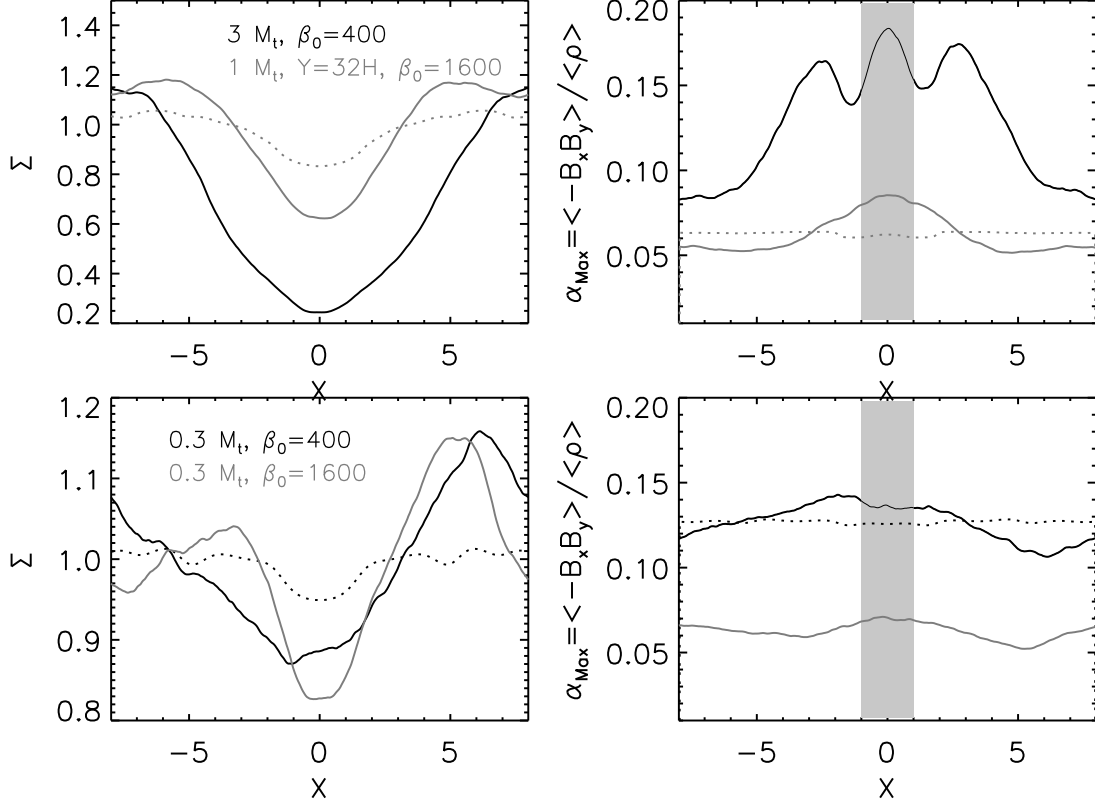


FIG. 10.— Similar to Figure 8 but for more MHD and viscous cases. Upper panels: the case with a more massive planet (M30B400), and a y-direction longer boxes (M10B1600b). The viscous case (V10bsv) is shown as the dotted curve. Bottom panels: the cases with a less massive planet and various net vertical field strengths (M03B400, M03B1600). The dotted curve is the viscous case V03. In all these cases, α of MRI disks peaks towards the gap region.

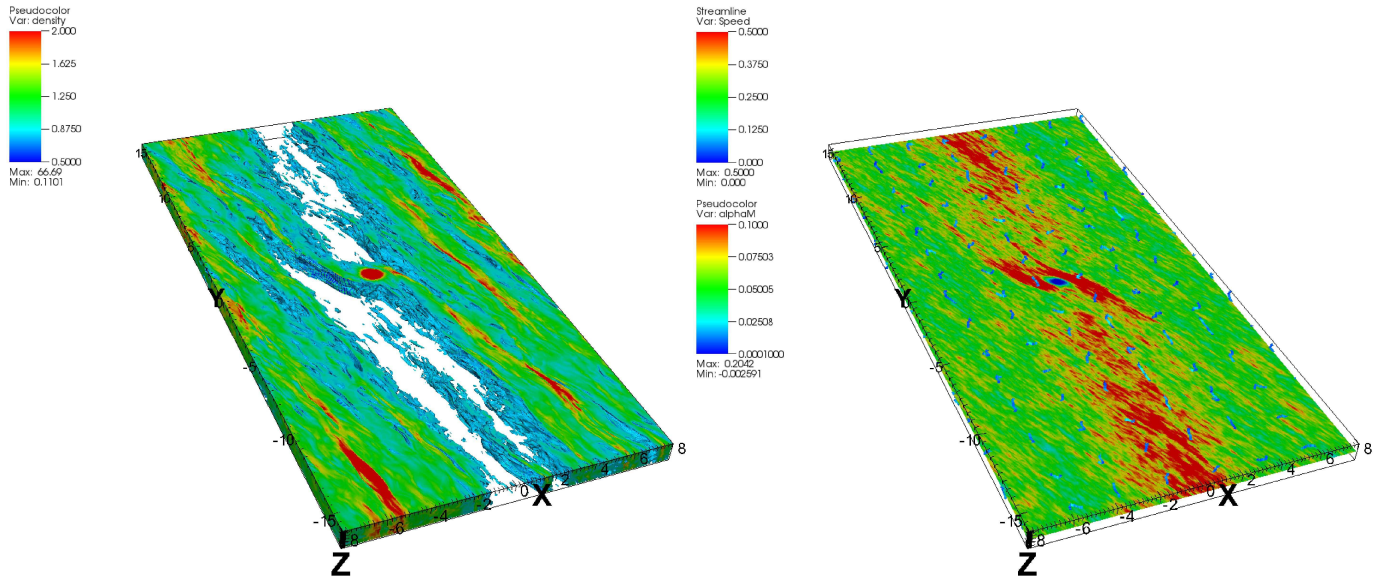


FIG. 11.— Left Panel: Volumetric rendering of the density during the interaction between the planet and MRI turbulent disks for M10B1600b. Regions with densities below 0.8 midplane density are removed. Right Panel: The time averaged α_{Max} at the $z=0$ slice for this case. The time averaged magnetic field streamlines are also plotted. The turbulent component of the magnetic fields is averaged out and the averaged fields show the net vertical field geometry. The net vertical magnetic fields in M10B1600 seem to diffuse freely into the gap, causing a higher α .

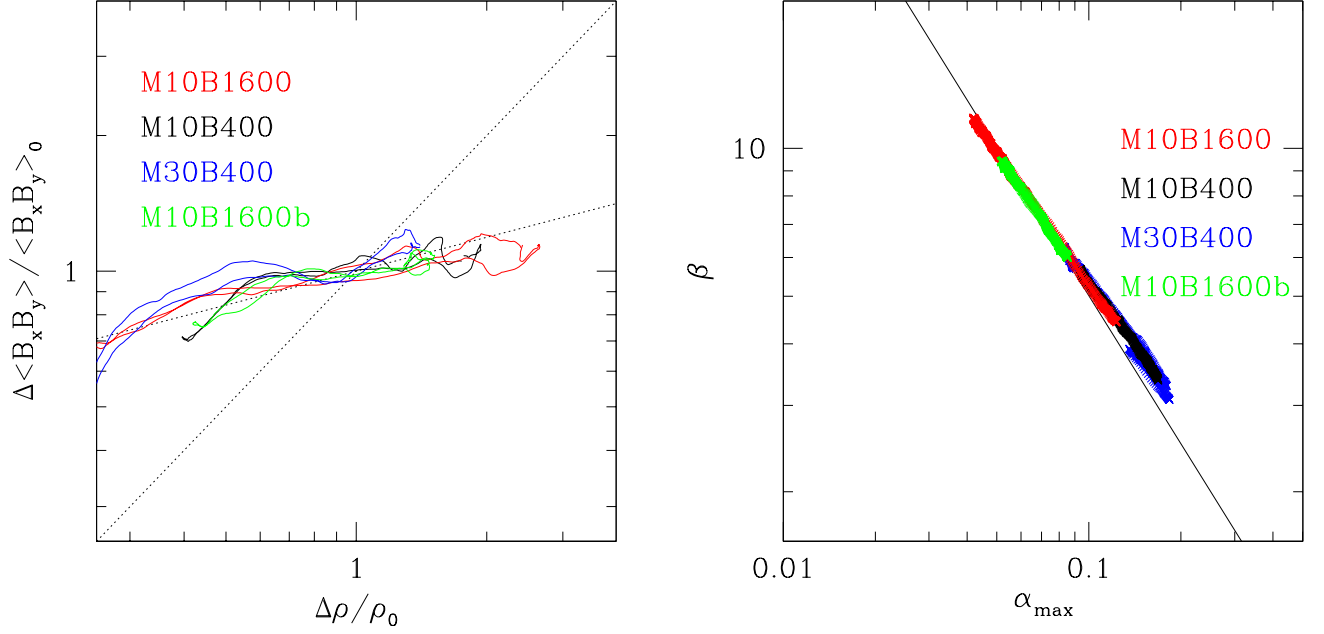


FIG. 12.— Left panel: the excess of the yz -direction and time averaged Maxwell stress with respect to the excess of the averaged density at each x position across the gap region for the M10B400 (black curves), M10B1600 (red curves), M30B400 (blue curves), and M10B1600b (green curves). $\langle B_x B_y \rangle_0$ is the Maxwell stress at the position where the averaged $\rho = \rho_0 = 1$. The dotted curve from the lower left to the upper right shows the stress-density relation in a viscous disk $\Delta T/T = \Delta \rho/\rho$, while the best fit for the stress across the gap in MRI disks is $\Delta T/T \propto 0.25 \Delta \rho/\rho$. Right panel: The yz -direction and time averaged β with respect to the averaged disk Maxwell stress α_{Max} at each x position across the simulation domain. The point moves to the lower right when it crosses the gap where it has lower β and higher α_{Max} . The solid line is $\beta = 1/2\alpha$.

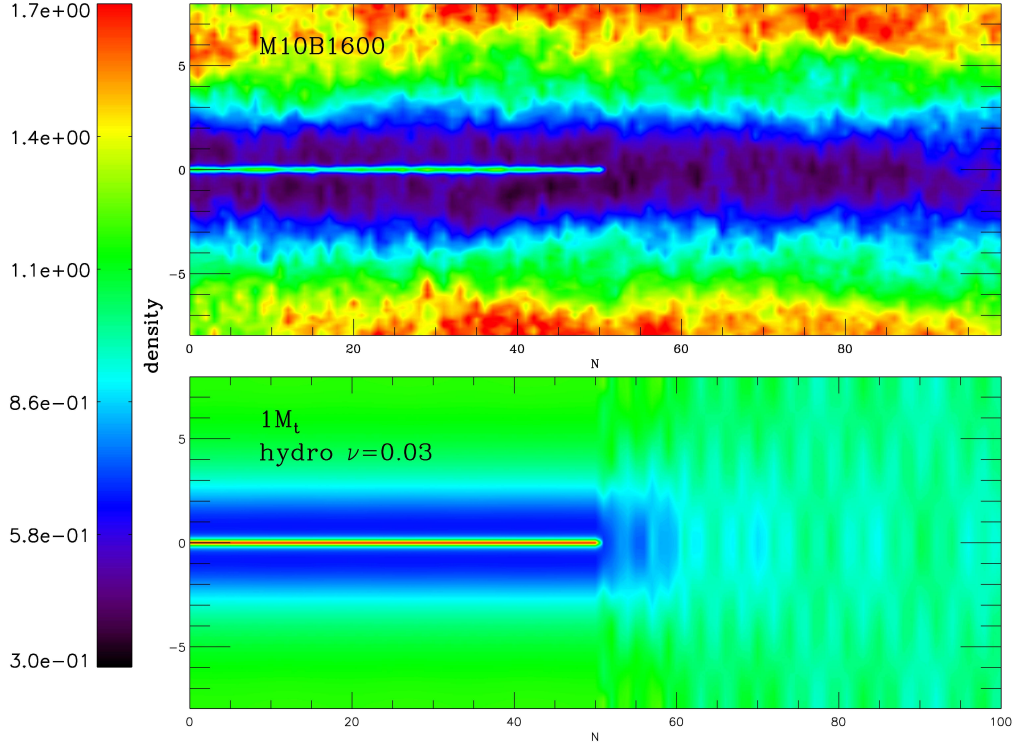


FIG. 13.— The space time plot for the yz -direction averaged disk surface densities for the M10B1600 (net vertical flux), and V10la (viscous HD). However, the planet's potential is suddenly changed to be zero in the middle of the simulation. As shown, the gap feature in M10B1600 persists longer than that in a viscous disk. This is consistent with the fact that the stress across the gap in MRI disks is more uniform than the density, so that any existing density feature takes a longer time to be altered by turbulent stress in net vertical flux MHD disks.

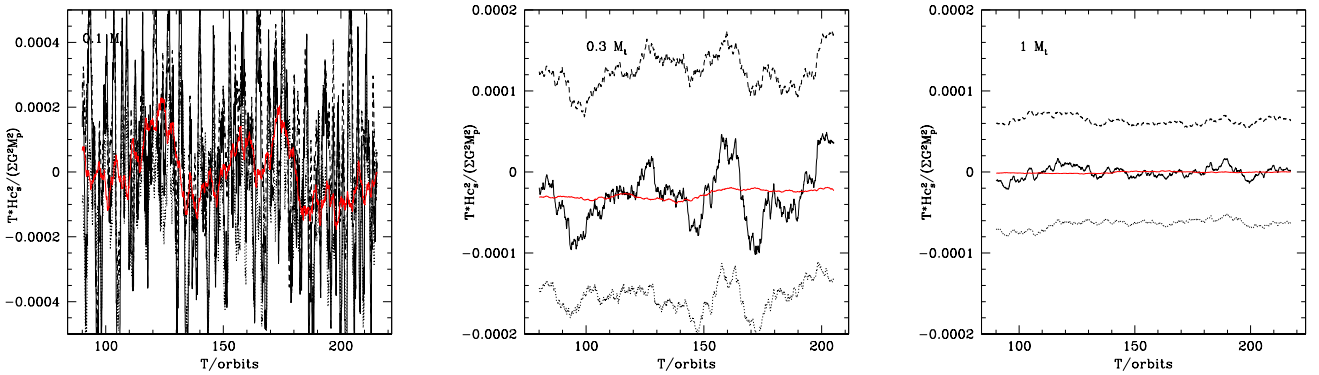


FIG. 14.— The integrated torques with time for M01B400 ($1 M_{th}$), M03B400 ($0.3 M_{th}$), M10B400 ($0.1 M_{th}$) (left to right panels). The dashed curves are the torques from $x > 0$ side of the disk while the dotted curves are from $x < 0$ side of the disk. The solid curves are the net torque. These curves are averaged over 1 orbit period. The red curves are the net torque averaged over 10 orbits period. For less massive planets, the torque due to the turbulence can dominate the Lindblad torque, leading to the planet's random walk. For the intermediate mass planet ($0.3 M_t$ case), the net torque is actually non-zero (negative in this case), contradictory to the expectation that, due to the symmetry of the shearing box, the averaged net torque should be zero. This non-zero net torque is caused by the non-uniform disk background from the large scale MRI zonal flow.